Investigation of electron source and ion flux uniformity in high plasma density inductively coupled etching tools using two-dimensional modeling

Peter L. G. Ventzek,[a] Michael Grapperhaus, and Mark J. Kushner[b]
University of Illinois, Department of Electrical and Computer Engineering, Urbana, Illinois 61801

(Received 23 May 1994; accepted 22 September 1994)

Inductively coupled plasma (ICP) sources are being developed as reactors for high plasma density (10^{11}–10^{12} cm^{-3}), low-pressure (<10–20 mTorr) etching of semiconductors and metals for microelectronics fabrication. Transformer coupled plasmas (TCPs) are one variant of ICP etching tools which use a flat spiral coil having a rectangular cross section powered at radio frequencies (rf) to produce a dense plasma in a cylindrical plasma chamber. Capacitive rf biasing of the substrate may also be used to independently control ion energies incident on the wafer. The uniformity of generating the plasma and the uniformity of the flux of reactants to the substrate are functions of the geometry and placement of the coil; and of the materials used in the construction of the chamber. In this article, we use results from a two-dimensional model to investigate design issues in TCPs for etching. We parametrize the number of turns and locations of the coil; and material properties of the reactor. We find that at low pressure, designs which produce ionization predominantly at larger radii near the edge of the wafer produce more uniform ion fluxes to the substrate. This results from a "converging" ion flux which compensates for losses to lateral surfaces. Careful attention must be paid to metal structures in the vicinity of the coils which restrict the azimuthal electrical field. This situation results in reduced power deposition at large radii, which can be compensated by over sizing the coil or by using auxiliary solenoidal coils. The plasma and neutral transport, dominated by diffusion, treats the advective flow from the gas inlets and pump port as local sources and sinks which are rapidly volume averaged.

I. INTRODUCTION

New reactors for plasma etching of semiconductor materials and metals for use in the fabrication of microelectronics devices are being developed which use lower gas pressures (<a few to tens of mTorr), and which operate with a low and controllable bias on the substrate.[1] These systems have less ion scattering which results in a more anisotropic flux of ions to the wafer. They also generate lower energy ions which may produce less damage to the wafer. Since the rate of radical generation is proportional to $k[e][N]$ (k is the electron impact rate coefficient, $[e]$ is the electron density, and $[N]$ is the gas density), lower gas pressure etching systems must operate at higher plasma densities to achieve the same processing rate as conventional high-pressure (10s–100s mTorr) reactive ion etching (RIE) systems.

Inductively coupled plasma (ICP) reactors are being developed for low gas pressure, high plasma density etching applications. Two classes of designs are being investigated. The first uses a solenoidal coil wrapped around the outer diameter of the chamber.[2] The second uses a spiral coil of rectangular cross section placed on the top of a cylindrical chamber.[3] The latter configuration is often referred to as a transformer coupled plasma (TCP). When the coil is driven at frequencies of a few to 10s of MHz with 100s of watts to a few kW of power deposition in the reactor, plasma densities of 10^{11}–10^{12} cm^{-3} are generated with gas pressures of 5–20 mTorr and flow rates of 10s–100s sccm.

The particular ICP geometry of interest, shown in Fig. 1, was jointly developed by IBM, East Fishkill, and LAM Research, Inc. The "stove-top" coil dominantly produces an azimuthal electric field which has a maximum in the plasma at approximately half the radius just under the dielectric roof. This results in a toroidally shaped power deposition. The low operating pressure results in dominantly diffusive transport which helps to homogenize the plasma and produce a fairly uniform flux to the substrate. A separate rf bias may be applied to the substrate to independently control ion energies onto the wafer.

A number of experimental investigations on TCP reactors have recently been reported. Reactors employing cusp magnets in a "magnetic bucket" to improve confinement of electrons have been experimentally investigated by Keller *et al.*,[4] Barnes *et al.*,[5] and O'Neill *et al.*[6] Keller *et al.*[4] have demonstrated that the ion density is linearly proportional to inductively coupled power deposition in CF_4, Ar, and O_2 plasmas at a gas pressure of 5 mTorr and power depositions of 300 W–2 kW. They also showed that dc self-bias on the substrate is not a sensitive function of the inductive power deposition for rf bias powers less than one third that of the inductive power. This demonstrated that ion generation and acceleration to the wafer could be separately controlled. Barnes *et al.*[5] performed Langmuir probe measurements of oxygen plasmas and showed that the peak negative ion densities were a few times the electron densities (0.2–10 mTorr, 1000 W). They also showed that the electron energy distributions were Maxwellian at low gas pressures (<0.5 mTorr) and resembled Druyvesteyn distributions at higher pressures (10 mTorr). The average electron temperatures increased from 6

[a]Present address: Department of Electrical Engineering, Hokkaido University, Sapporo 060, Japan.
[b]Author to whom correspondence should be addressed.

 0734-211X/94/12(6)/3118/20/$1.00

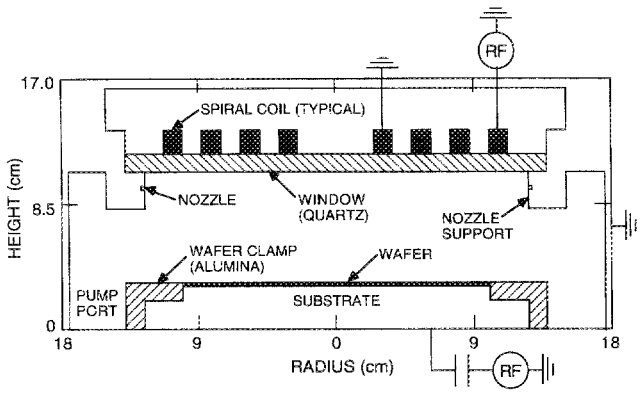

FIG. 1. Schematic of the standard ICP reactor. The spiral coil and substrate are driven at 13.56 MHz. The substrate-to-window distance is 7.5 cm. Gas is injected radially inward through nozzles. The pump ports, asymmetric in the actual device, are modeled as an annular ring.

to 20 eV as the pressure was decreased from 10 to 0.5 mTorr with an inductive power deposition of 1000 W. O'Neill *et al.*[6] observed Doppler broadening of ion emission to measure ion temperatures in the bulk of argon plasmas and obtained values as high as 0.25 eV.

Commercial reactors which do not use magnetic buckets have been investigated by Patrick *et al.*[7] and Carter *et al.*[8] Patrick *et al.*[7] measured plasma uniformity using Langmuir probes in Ar or Cl_2 plasmas in the LAM 9400 reactor. They found that uniformity decreased with increasing coil power. They also found that the dc self-bias was a function of both inductively coupled power and rf bias power applied to the substrate over large dynamic ranges in either quantity. They also investigated the effect of bias power on damage to the wafer. Carter *et al.*[8] studied etching of SiO_2 and polycrystalline silicon (p-Si) in the LAM 9400 reactor. They suggested that the rate-limiting process in polysilicon etching is availability of the chlorine radical, and demonstrated the use of bias and pressure to control microloading effects in etching 0.4-μm features.

Other reactor configurations have also been investigated by Hopwood *et al.*,[1,9–11] Wendt *et al.*,[12,13] Mahoney *et al.*,[14] Beale *et al.*,[15] and Fusakawa *et al.*[16] Hopwood[1,9–11] used microwave interferometry, Langmuir probes, and a gridded energy analyzer to investigate plasma properties in a reactor using planar coils having a rectangular (as opposed to circular) layout. He characterized the toroidal nature of the electromagnetic field and demonstrated the enhancement of the plasma uniformity with the addition of a magnetic bucket to the reactor. Wendt and co-workers[12–15] investigated a reactor similar to the LAM design and demonstrated an extension of the operating regime of the reactor through pulsed operation. In these works, Langmuir probe measurements and optical emission spectroscopy were used to characterize the spatial distributions of electron temperature, excited states, and plasma density. They found that maximum plasma emission and maximum in electron temperature occurred in the toroidally shaped region corresponding to maximum power deposition. At moderate aspect ratios the plasma density was maximum on the axis, a consequence of the dominance of diffusion in ion transport at the low pressures of interest. At large aspect ratios (squat reactors) the plasma had off axis maxima. Fusakawa *et al.*[16] investigated the effect of inductive power and rf bias power applied to the substrate on the dc self-bias. They found that a negative dc bias increased to more positive values with increasing inductive power deposition. They also investigated the effect of different antenna configurations on the plasma uniformity. They showed that an antenna having a single turn at a large radius produced a plasma having improved radial uniformity compared to a nested multiple turn antenna. Finally, etch rates of 1–3 μm/min have been demonstrated for various gas mixtures and substrates; oxygen etching of photoresist,[4] SF_6–CCl_2F_2 etching of Si,[4] Cl_2–O_2 etching of Si and SiO_2,[8] and Cl_2 etching of Si.[7]

These works have shown that the uniformity of plasma generation and of the etching fluxes to the substrate are functions of the design of the coil and of the materials used in the construction of the chamber. Clearly, power deposition is maximum in the vicinity of the coils; and hence, coils located at larger radii tend to produce plasmas whose source is at large radii. However, the details of the materials in the vicinity of the coil are also important in determining the uniformity of plasma generation. Metal materials which confine the electric field to, for example, smaller radii ultimately produce less uniform ion fluxes to the substrate. Advective gas flow is of secondary importance with respect to plasma uniformity at low pressures where transport is diffusive or quasimolecular. Advective gas flow at the pressures of interest provides "sources and sinks" of feed stock gases and products which are rapidly volume averaged by diffusion. The details of the gas inlets may be an important consideration in producing uniform radical sources at high power deposition where there is depletion of the feed stock gases.

To investigate design issues with respect to producing uniform plasmas and reactant fluxes to the substrate, a computer model has been developed. The model is a hybrid simulation[17–19] which combines an electromagnetic module, an electron Monte Carlo simulation, and a hydrodynamic simulation to obtain species densities and fluxes as a function of position (r,z). The model will be described in Sec. II followed by a comparison of results from the model to experiments in Sec. III. Using results from the model, we will discuss design issues for ICPs in Sec. IV. Our concluding remarks are in Sec. V.

II. DESCRIPTION OF THE MODEL

The radially and axially varying power deposition in ICP reactors requires that design issues be addressed by two-dimensional (2D) models. In this regard, a number of 2-D models for ICP reactors have recently been developed. Paranjpe[20] developed a fluid model in which the azimuthal electric field is obtained by solution of Maxwell's equations while assuming that electric fields in the plasma can be described by ambipolar diffusion. By using a Maxwellian electron energy distribution his model executes very rapidly and so is well suited to design studies. He found that the ion flux to the wafer can be controlled by design of the coil and shape of the dielectric window. For example, conical antennas

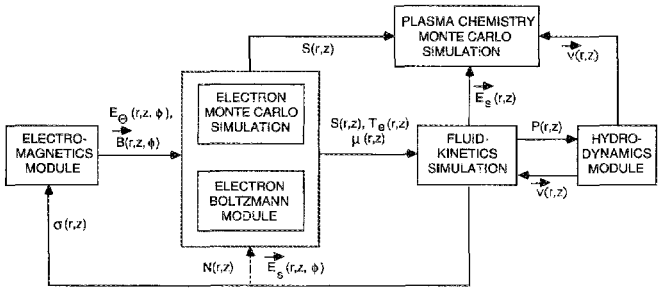

FIG. 2. Schematic of the hybrid model showing the information flow between the modules. The electron Boltzmann module is used for higher pressure applications and will be discussed in a future publication.

which place the center turns further from the window produce plasmas having lower densities on axis. Stewart *et al.*[21] have developed a three-moment fluid model for ICP reactors. Transport coefficients are functions of the local electron temperature obtained from the energy equation. By parametrizing the location of power deposition, they demonstrated scaling laws for obtaining uniform plasmas for different pressures and power depositions. In an improvement to that model, Stewart *et al.*[22] have incorporated a self-consistent solution for the azimuthal electric field developed by Jaeger and Berry,[23] and have studied alternate coil configurations. Bartel *et al.* have used a DSMC (direct simulation Monte Carlo) model to investigate radical and ion transport in ICP reactors using solenoidal coils.[24]

The model used in this study is an improvement to that discussed in Refs. 18 and 19. Therefore, the basis of the model will be only briefly discussed and emphasis will be placed on improvements to the previously described model. Our model for ICP reactors is a 2D [cylindrically symmetric (r,z)] hybrid simulation consisting of an electromagnetic module (EMM), an electron Monte Carlo simulation (EMCS), a fluid-chemical kinetics simulation (FKS), a hydrodynamic model (HM), and an off-line plasma chemistry Monte Carlo simulation (PCMCS).

A schematic of the hybrid model is shown in Fig. 2. The simulation begins by calculating the coil generated electric and magnetic fields $[E(r,z,\phi)$ and $B(r,z,\phi)]$ as a function of position and phase during the radio frequency (rf) cycle using the EMM. To initially obtain these fields, we estimate the plasma conductivity $\sigma(r,z)$. These fields are then used in the EMCS for electron trajectories. In the EMCS, the time averaged electron energy distribution $f(\epsilon,r,z)$ is obtained by advancing and recording electron trajectories over $\approx$50 rf cycles using the fields from the EMM. During the first iteration of the model, electrostatic fields $E_s(r,z,\phi)$ are estimated. $f(\epsilon,r,z)$ is then used to calculate source functions for electron impact processes $S_j(r,z)$, diffusion coefficients $D(r,z)$, mobilities $\mu(r,z)$, and average electron temperatures $T_e(r,z)$.

The source functions and transport coefficients are then used in the FKS which solves for the densities of all charged and neutral species, and for the electrostatic plasma potential. The FKS is integrated for 10s to 100s of rf cycles. An acceleration algorithm is employed to speed the convergence of the FKS, and Poisson's equation is solved using a semi-implicit technique, both of which are described in Ref. 19. The time averaged conductivities are then transferred to the EMM. $E_s(r,z,\phi)$ and time averaged species densities are transferred to the EMCS. The modules are iterated again, beginning with the EMM, until the cycle averaged plasma densities in the FKS converge.

After the model converges, the source functions (cm^{-3} s^{-1}) of ions and radicals generated in the EMCS, and $E_s(r,z,\phi)$ produced in the FKS are used in a separate plasma chemistry Monte Carlo simulation. In the PCMCS, the trajectories of ions and radicals are followed throughout the reactor while accounting for elastic and charge exchange collisions as well as chemical reactions. The end results are the ion fluxes and ion energy distributions as a function of position on the wafer. Improvements to the previously described model will now be discussed.

A convenient mechanical improvement to the model was to implement a preprocessor we call the material-mesh definer (MMD). The MMD is a simple utility which enables us to quickly define the geometry and material properties on a rectilinear (r,z) grid. The MMD produces arrays which define the materials as a function of position, material properties, boundaries between materials, and the orientation of the normal of each boundary. The output of the MMD was incorporated into each of the modules of the hybrid model. All algorithms in the hybrid model were rewritten to be totally general using stencils from the MMD which select (or mask out), for example, powered metal surfaces. Using this methodology all input parameters (e.g., reactive sticking coefficients) are specified not on a geometrical basis but rather on a material basis.

In the former model, the electromagnetic fields from the EMM were solved only in the body of the plasma using a technique introduced by Yu and Girshick.[25] We now solve for $E(r,z,\phi)$ and $B(r,z,\phi)$ in the entire volume of the reactor; and in this way are better able to account for the consequences of geometry and materials on the electromagnetic fields. We solve the following forms of Maxwell's equations;

$$\nabla\times\mathbf{E}=-\frac{\partial\mathbf{B}}{\partial t}, \tag{1a}$$

$$\nabla\times\mathbf{H}=\mathbf{J}+\frac{\partial\mathbf{D}}{\partial t}, \tag{1b}$$

$$\nabla\cdot\mathbf{D}=\rho. \tag{1c}$$

Using the assumption of charge neutrality ($\rho=0$) and $\mathbf{J}=\sigma\mathbf{E}$, we take the cross product of Eq. (1a) and obtain

$$\nabla\cdot\frac{1}{\mu}\nabla\mathbf{E}=\frac{\partial^2(\epsilon\mathbf{E})}{\partial t^2}+\frac{\partial(\sigma\mathbf{E}+\mathbf{J}_0)}{\partial t} \tag{2}$$

in Eq. (2), we used the identities $\mathbf{J}=\sigma\mathbf{E}$, and $\mathbf{B}=\mu\mathbf{H}$. J_0 represents driven currents in, for example, the coils. All quantities are complex.

We assume that the coil current is driven harmonically at frequency ω (rad/s) and that the electric field is also harmonic;

$$\mathbf{J}_0(\mathbf{r},t)=j_0(\mathbf{r})e^{i\omega t}, \tag{3a}$$

$$\mathbf{E}(\mathbf{r},t)=E(\mathbf{r})e^{i\omega t}. \tag{3b}$$

We allow $J_0=j_{0r}+ij_{0i}$ to be complex to account for coil-to-coil phase differences in the current. This may occur "naturally" or as a result of separately powering the coils. The plasma conductivity is given by

$$\sigma(\mathbf{r})=\sum_l \sigma_l(\mathbf{r}), \tag{4a}$$

$$\sigma_l(\mathbf{r})=\frac{q^2 n_l(\mathbf{r})}{m_l}\frac{1}{(\nu_{ml}+i\omega)}=\sigma_{rl}(\mathbf{r})+\sigma_{il}(\mathbf{r}), \tag{4b}$$

$$\sigma_{rl}=\frac{q^2 n_l}{m_l \nu_{ml}}\frac{1}{(1+\omega^2/\nu_{ml}^2)}, \quad \sigma_{il}=-\sigma_{rl}\frac{i\omega}{\nu_{ml}}. \tag{4c}$$

The sums in Eqs. (4) are over charged species in the plasma, having density n, mass m, and momentum transfer collision frequency ν_m. The collision frequency of electrons is a function of the local electron energy distribution as generated by the EMCS. To that degree, ν_m includes the effect of the rf magnetic field on electron transport. Explicit dependence of the rf magnetic field on the conductivity is not otherwise included. The subscripts i and r denote real and imaginary components. The spatially dependent plasma densities and collision frequencies are provided by the FKS and EMCS modules. In practice, only the electrons significantly contribute to the conductivity, and so the index for plasma species will be suppressed. The conductivities of nonplasma materials are simply specified and assumed to be real. The permittivity of the plasma is

$$\epsilon(\mathbf{r})=\epsilon_0\left(1-\frac{\omega_p^2/\omega^2}{(1-i\nu_m/\omega)}\right)=\epsilon_r+i\epsilon_i, \tag{5}$$

where $\omega_p=(nq^2/m\epsilon_0)^{1/2}$ is the plasma frequency. The permittivities of nonplasma materials are simply specified and assumed to be real. The magnetic permeabilities of all materials are also simply specified.

With these definitions, we constructed two equations for the real and imaginary components of the amplitude of the electric field, $\mathbf{E}(\mathbf{r})=\mathbf{E}_r(\mathbf{r})+\mathbf{E}_i(\mathbf{r})$

$$-\nabla\cdot\frac{1}{\mu}\nabla\mathbf{E}_r=\omega^2(\epsilon_r\mathbf{E}_r-\epsilon_i\mathbf{E}_i)+\omega\sigma_r\mathbf{E}_i+\omega\sigma_i\mathbf{E}_r+\omega j_{0i}, \tag{6a}$$

$$-\nabla\cdot\frac{1}{\mu}\nabla\mathbf{E}_i=\omega^2(\epsilon_r\mathbf{E}_i-\epsilon_i\mathbf{E}_r)-\omega\sigma_r\mathbf{E}_r+\omega\sigma_i\mathbf{E}_i-\omega j_{0r}. \tag{6b}$$

If we assume that the spiral coil can be represented by nested circular coils, the symmetry of the reactor results in there being only an azimuthal component of the coil current and of the electric field. We, therefore, keep only the azimuthal component of Eqs. (6). The (r,z) components of the electric field which results from the inductive voltage drop across the coil are addressed in the FKS.[19] Equations (6) are simultaneously solved using the method of successive-over-relaxation with a relaxation parameter of $\alpha=1.3$. The solution is declared converged if the relative difference in either component of the electric field at any point in the reactor after ten successive iterations, $\Delta|E|/|E|$, is less than 10^{-6}.

The boundary condition on the axis of symmetry ($r=0$) is $E=0$. The boundary condition on (noncoil) metallic surfaces were handled in either of two ways. The first was to simply set $E=0$ on all nondriven metal surfaces. The second was to specify the actual conductivities and permittivities of the metals and allow the code to calculate the electric field. Using the latter method, the electric field does not penetrate beyond the first computational cell and so the result is essentially the same as specifying that $E=0$ on nondriven metal surfaces. However, the advantage of the latter method is that one can approximate heating of metal structures located near the coils. We, typically, specify the total desired power deposition by the inductively coupled field in the plasma and other materials. We then adjust the coil current to obtain this value of power deposition.

The skin depth for penetration of the electric field into the coils (<10 μm) is smaller than our mesh size, and so we cannot explicitly resolve the electric field and current density in the coil. We handle the electric field in the coil using the following method. The total current through the coil is specified. We then define a conduction current density through the cross section of the coil which is restricted to a specified depth of the surface of the coil. The computational cell just interior to the surface of the coil is redefined to have this depth. The boundary condition for the azimuthal electric field on the interior boundary of this computational cell is $\partial\mathbf{E}/\partial\mathbf{n}=0$, where $\mathbf{n}$ is the normal to the interior of the surface. This boundary condition is equivalent to assuming total reflection of the interior traveling wave. The solution for the electric field is otherwise the same as elsewhere in the reactor. In practice the width of the computational cell under the surface of the coil is ≈ 0.1 that of the exterior cells. We parametrized the width of the surface cell over a large range of thicknesses. Although the electric field in the surface cell is a sensitive function of the width of the surface cell, the electric field more than a few computational cells away from the coils is insensitive to the width of the surface cell.

The electron Monte Carlo simulation module is essentially the same as described in Ref. 19 with the following exceptions. The EMCS now incorporates the MMD methodology. This enables us to quickly place and remove electron pseudoparticles based on the material property of the computational cell they occupy. The EMCS now also uses separate random number generators for obtaining spatial positions, speeds, scattering angles, collisions and secondary electron energies (a total of 13 separate generators). The separate generators help to insure a uniformly distributed random function for each physical phenomenon.

Stochastic electron heating can be a significant power source in low-pressure ICPs as electrons flow into and out of the inductive skin depth. The EMCS captures this behavior since the electron pseudoparticles respond to the time and spatially varying electric fields in a fully kinetic fashion. There may, however, be an inconsistency between the electron energy distribution and the power deposition calculated in the EMM, since the latter quantity is the collisional value

obtained from the volume integral of σE^2. This issue is further discussed in Sec. IV A.

The amplitude of the rf magnetic field in the plasma, typically, does not exceed 20 G, and averages <10 G in the inductive skin depth. This corresponds to a maximum electron cyclotron frequency of 5.6×10^7 s^{-1} and an average frequency throughout the skin depth of about 10^7 s^{-1}. The minimum Larmor radius is 2.5–3 cm, which is commensurate to or exceeds the skin depth. The cycle averaged cyclotron frequency is nearly the same as the rf frequency while the direction of the electron acceleration reverses during the rf cycle. The end result is that for the conditions of interest, the effect of the rf magnetic field on electron source functions and average energies is small. We have run the EMCS with and without the acceleration terms due to the rf magnetic field, and obtained nearly identical results. The majority of the results shown here do not include the rf magnetic field in the EMCS.

The fluid-chemical kinetics simulation is also functionally the same as described in Ref. 19 with the following improvements. The FKS now incorporates the MMD methodology which allows boundary conditions to be specified in a more general and flexible manner. Using this procedure, the reactive sticking coefficient r_s for neutral and charged species is specified by the material they strike. For example, r_s for Cl is defined as

$$\begin{aligned} \mathrm{Cl}\rightarrow\text{stainless steel} &\xrightarrow{r_s=0.005} 0.5[\mathrm{Cl_2}] \\ &\xrightarrow{r_s=0.995} \mathrm{Cl}, \end{aligned} \tag{7a}$$

$$\mathrm{Cl}\rightarrow\text{wafer} \xrightarrow{r_s=0.05} 0.25[\mathrm{SiCl_4}]. \tag{7b}$$

These conditions are then applied only to material boundaries between [plasma, stainless steel] or [plasma, wafer] as denoted by the boundary arrays produced by the MMD.

In the previously described model, Poisson's equation was solved only within the volume of the plasma using a semi-implicit technique. Boundary conditions were specified by lining the plasma with either metals or dielectrics of given thickness, and calculating charge accumulation on the surface of the dielectric. Now, using the materials properties identified by the MMD, Poisson's equation is solved throughout the volume of the reactor. The form of Poisson's equation we solve is

$$\nabla\cdot\epsilon(\mathbf{r})\nabla\Phi(\mathbf{r})=-[\rho(\mathbf{r})+h(\mathbf{r})\rho'(\mathbf{r})], \tag{8}$$

where Φ is the electric potential, ϵ is the local permittivity of the material, ρ is the volumetric charge density, and ρ' is an effective charge density which accounts for the surface charging of dielectrics. $h(r)$, produced by the MMD, is a stencil which selects mesh points which are on the boundary between the plasma and dielectrics.

ρ' is an effective charge density which is obtained by spreading the surface charge on the dielectric through the finite width of the computational cell centered on the surface. This method is described by Morrow.[26] The surface charge density σ_s is obtained by integrating (in time) the total flux of charged species to the surface

$$\rho'(t)=\frac{1}{\Delta r}\sum_j \int_0^t eq_j\varphi_j(t')dt', \tag{9a}$$

$$\varphi_j=(q_j\mu_jN_j\mathbf{E}-D_j\nabla N_j)\hat{n}. \tag{9b}$$

The sum in Eq. (9a) is over charged species j in the plasma, having flux to the surface ϕ_j, density N_j, mobility μ_j, and diffusion coefficient D_j. $\mathbf{E}$ is the electrostatic field at the surface having normal $\hat{n}$, and q_j is the charge of the species (in units of e).

The boundary conditions for Poisson's equation are obtained by specifying the instantaneous potential on all grounded or electrically driven surfaces. Floating metal surfaces are treated identically to dielectrics by specifying an appropriate ϵ and averaging the collected charge over the surface of the metal. Using the MMD, all electrically driven metal surfaces are assigned a voltage, frequency, and phase. The inductive voltage drop across the coil is specified on a turn-by-turn basis.

The circuit is represented in the same manner as in Ref. 19 where a blocking capacitor is placed in series with the voltage generator for all rf driven metals. The instantaneous charging current to the blocking capacitor is obtained from

$$I(t)=\int m(\mathbf{r}')\left(\sum_j eq_j(q_j\mu_jN_j\mathbf{E}-D_j\nabla N_j)+\frac{\partial\mathbf{D}}{\partial t}\right)\cdot\hat{n}\,dA(\mathbf{r}'), \tag{10}$$

where the integral is over the surfaces forming the boundary between the plasma and contact materials. $m(\mathbf{r})$ is a stencil (defined by the MMD) which selects mesh points at this boundary. $m(\mathbf{r})$ has values $(0,1,-1)$ to denote mesh points which are either not at a boundary, mesh points at the boundary for materials which are electrically on the ground side of the capacitor, and boundary mesh points for materials which are electrically on the powered side of the capacitor.

Although gas flow is in the quasimolecular flow regime at the low gas pressures of interest, the locations of inlet nozzles and pump ports may nevertheless be important considerations in optimizing the uniformity of radical fluxes to the substrate when operating at high power deposition where the feed stock gases are depleted. In the previous model, flow was included as a residence time effect. That is, the continuity equations included a source and sink whose time scales were determined by the net gas flow through the system and the volume of the chamber

$$\frac{\partial N_j}{\partial t}=\frac{N_{ij}}{\tau_1}-\frac{N_j}{\tau_0}. \tag{11}$$

In Eq. (11), N_{ij} is the inlet density of species j. N_j is the reactor averaged densities of neutral species j. The inlet residence time is $\tau_1=VP/F$, where F is the total flow rate (molecules/s), V is the volume of the chamber, and P is the gas pressure. The exit residence time τ_0 is dynamically chosen so that the chamber gas pressure remains a specified

value. Under conditions where the feed stock gases are significantly dissociated, $\tau_0 < \tau_i$ since $\Sigma_j N_{ij} < \Sigma_j N_j$.

In the results presented here, an advective flow field computed in the hydrodynamic model is included in the transport terms of the continuity equations for neutral minor species in the FKS. The transport therefore includes both advective and diffusive terms

$$\frac{\partial N_j}{\partial t} = -\nabla\cdot(\mathbf{v}N_j - D_j\nabla N_j), \tag{12}$$

where $\mathbf{v}$ is the velocity of the advective flow field. The advective field was obtained by solving the fully compressible fluid conservation equations:

$$\frac{\partial \rho}{\partial t} = -\nabla\cdot(\rho\mathbf{v}), \tag{13a}$$

$$\frac{\partial(\rho\mathbf{v})}{\partial t} = -\nabla P - \nabla\cdot(\rho\mathbf{v}\mathbf{v}) - \nabla\cdot\bar{\bar{\tau}}, \tag{13b}$$

$$\frac{\partial(\rho c_v T)}{\partial t} = H_J + \nabla\cdot\kappa\nabla T - \nabla\cdot(\rho c_v T\mathbf{v}) - P\nabla\cdot\mathbf{v} + \Gamma, \tag{13c}$$

where ρ is the mass density, P is the thermodynamic pressure, $\bar{\bar{\tau}}$ is the viscosity tensor, H_J is the Joule heating from the plasma, κ is the thermal conductivity, and Γ is the dissipative heating term. The forms of $\bar{\bar{\tau}}$ and Γ we used are as given by Thompson.[27] To account for long mean-free-path transport, we used slip boundary conditions, as described by Thompson.[27] We compared our computed advective flow field to results obtained with flow fields produced using a DSMC method.[28] The important flow field characteristics were captured using our method.

Using an advective flow field obtained using fluid conservation equations is clearly an approximation at the low pressures of interest. Since diffusion speeds of neutrals (10^3–10^4 cm/s) usually greatly exceed the advective velocities (10^2–10^3 cm/s) except at the nozzle entrance, the advective velocity in Eq. (12) does not significantly affect the volumetric densities. The advective terms functionally serve as local sources and sinks of molecules at the nozzle and pump port which are rapidly volume averaged by diffusion. To insure that we retain the mass conservation which is produced by the HM, the diffusion boundary conditions at the inlets and outlets are $D\nabla N = 0$.

In this work we have investigated Ar/Cl_2 chemistries as used in the etching of Al and polycrystalline silicon (p-Si). The species included in the model are listed in Table I and the reactions included in the model are shown in Table II.[29–39] To reduce the magnitude of the calculation in the FKS, we have lumped excitation to all excited states of Ar into an effective rate for excitation of Ar($4s$). Similarly, we have lumped excitation of all excited states of Cl into an effective rate of excitation of Cl* [effectively Cl($4s$)]. The appropriate energy loss collisions for excitation of all electronic states were included in the EMCS. Although we have not distinguished between Cl_2 and $Cl_2(v)$ in the FKS, the appropriate energy loss collisions for electrons are included in the EMCS. The fact that $Cl_2(v)$ is not included in the FKS results in the exclusion of superelastic collision of electrons with $Cl_2(v)$ in the EMCS. $SiCl_4$ is included as an etch product; however, further reactions of $SiCl_4$ in the gas phase have not been included.

TABLE I. Species included in the model (FKS module).

Species	Lennard-Jones parameters (neutral species)[a]	
	ϵ(K)	$\sigma(10^{-16}$ cm$^2)$
Ar	93.3	3.542
Ar*[b]	93.3	3.542
Ar^+		
Cl_2	316	4.217
Cl_2^+		
Cl	130.8	3.613
Cl^+		
Cl*[c]	130.8	3.613
Cl^-		
$SiCl_4$	390.2	5.977
e		

[a]Lennard-Jones parameters were obtained from R. A. Sveha, NASA Technical Report No. R-132, 1962.
[b]In the FKS, all excitation of Ar is lumped into Ar*, which is effectively Ar($4s$). See Table II for individual processes.
[c]In the FKS, all excitation of Cl is lumped into Cl*, which is effectively Cl($4s$). See Table II for individual processes.

For the gas mixtures of interest (Ar/Cl_2 with 10%–30% chlorine), electron impact processes produce Ar and Cl excited states and ions in roughly the same proportions. Following the initial electron impact excitation, charge exchange reactions between Ar^+ and Cl_2 (Cl) then produce Cl_2^+(Cl^+). Excitation transfer reactions between Ar* and Cl_2 produce Cl_2^+ (Refs. 40 and 41) whereas excitation transfer reactions between Ar* and Cl produce Cl*.[41,42] At high pressure, excitation reactions between Ar* and Cl/Cl_2 typically form excimers such as ArCl*. However, the lack of a stabilizing third body at the low gas pressures of interest results in a low production of excimer species. Although the pressures of interest (2–15 mTorr) are in the quasimolecular flow regime, the mean-free paths for Ar* and Ar^+ excitation transfer collisions with Cl_2 and Cl are commensurate with the transverse dimensions of the reactor. Ar* and Ar^+ are, therefore, depleted resulting in the dominant ions being Cl_2^+ and Cl^+. Due to the lack of a stabilizing third body, the rate of attachment to Cl is negligible. Significant attachment occurs only to Cl_2 and, therefore, the electronegativity of the plasma is a sensitive function of the fractional dissociation, as discussed by Lee *et al.*,[47] and Deshmukh and Economou.[48]

Neutral diffusion coefficients and mobilities were calculated using Lennard-Jones parameters following the methodology of Hirschfelder, Curtis, and Bird.[49] The Lennard-Jones parameters we used are listed in Table I. The mobilities for Ar^+ and Cl^- in Ar as a function of ion temperature were obtained from Ellis, Pai, and McDaniel.[50] The momentum transfer cross section for Ar^+ on Cl and Cl_2 was estimated to be 100×10^{-16} cm^2. The same value was used for Cl^+ and Cl_2^+ on Ar, Cl, and Cl_2. The mobilities of the neutral or charged species j in gas mixtures was obtained from

TABLE II. Reactions included in the model.

Reaction	Module[a]	Rate coefficient[b]	Reference
	Electron impact reactions		
$e+Ar \rightarrow Ar+e$	EMCS	c	29
$e+Ar \rightarrow Ar(4s)+e$	EMCS,FKS	c	30,d,e
$e+Ar \rightarrow Ar(4p)+e$	EMCS,FKS	c	30,e
$e+Ar \rightarrow Ar^- +e+e$	EMCS,FKS	c	31
$e+Ar(4s) \rightarrow Ar^+ +e+e$	EMCS,FKS	c	32
$e+Ar^+ \rightarrow Ar^* +e$	EMCS	c	33
$e+Cl_2 \rightarrow Cl_2+e$	EMCS	c	34
$e+Cl_2 \rightarrow Cl_2(v)+e$	EMCS	c	34
$e+Cl_2 \rightarrow Cl^- + Cl$	EMCS,FKS	c	34
$e+Cl_2 \rightarrow Cl_2+e$	EMCS	c	34
$e+Cl_2 \rightarrow Cl_2(C^1\Pi) \rightarrow Cl+Cl+e$	EMCS,FKS	c	34
$e+Cl_2 \rightarrow Cl_2(B^3\Pi,2^1\Pi,2^1\Sigma)+e$	EMCS	c	34
$e+Cl_2 \rightarrow Cl_2^+ +e+e$	EMCS,FKS	c	34
$e+Cl_2^+ \rightarrow Cl_2^* +e$	EMCS	c	33
$e+Cl_2^+ \rightarrow Cl^* + Cl$	EMCS,FKS	c	35,f
$e+Cl \rightarrow Cl+e$	EMCS	c	36
$e+Cl \rightarrow Cl(4s,4p,3d,5p,4d,5p)+e$	EMCS,FKS	c	36,d,g
$\leftrightarrow Cl^* +e$	EMCS,FKS		
$e+Cl \rightarrow Cl^+ +e+e$	EMCS,FKS	c	36
$e+Cl^* \rightarrow Cl^* +e$	EMCS	c	h
$e+Cl^* \rightarrow Cl^+ +e+e$	EMCS,FKS	c	37
$e+Cl^- \rightarrow Cl+e+e$	EMCS,FKS	c	38
	Heavy particle reactions		
$Ar^* + Ar^* \rightarrow Ar^+ + Ar+e$	FKS	5×10^{-10}	39
$Ar^* + Cl_2 \rightarrow Cl_2^+ + Ar+e$	FKS	7.1×10^{-10}	40,41
$Ar^* + Cl \rightarrow Cl^* + Cl$	FKS	7.0×10^{-10}	41,42
$Ar^+ + Cl_2 \rightarrow Cl_2^+ + Ar$	FKS	8.4×10^{-11}	43
$\rightarrow Cl^- + Cl + Ar$	FKS	6.4×10^{-11}	
$Ar^+ + Cl \rightarrow Cl^+ + Ar$	FKS	2.0×10^{-10}	i
$Cl^- + M^+ \rightarrow Cl+M$	FKS	1×10^{-7}	44,i
$(M=Cl^-, Cl_2^+, Ar^+)$			
$Cl^+ + Cl_2 \rightarrow Cl_2^+ + Cl$	FKS	5.4×10^{-10}	45
$Cl+Cl+Cl_2 \rightarrow Cl_2+Cl_2$	FKS	5.4×10^{-32} cm^6 s^{-1}	46
$Cl+Cl+Ar \rightarrow Cl_2+Ar$	FKS	1.3×10^{-32} cm^6 s^{-1}	46
$Cl^* \rightarrow Cl$	FKS	1×10^{5} s^{-1}	i

[a]Module of the hybrid in which this process occurs. EMCS=electron Monte Carlo simulation, FKS=fluid kinetics simulation.
[b]Rate coefficients have units of cm^3 s^{-1} unless noted otherwise.
[c]Rate coefficients are calculated from electron energy distribution obtained from the EMCS. See noted reference for cross section.
[d]Reverse reaction by detailed balance.
[e]All excitation is lumped into Ar* [effectively Ar(4s)] in FKS.
[f]Used same cross section as for $e+N_2^+ \rightarrow N^* + N$. See Ref. 35.
[g]All excitation is lumped into Cl* [effectively Cl(4s)] in FKS.
[h]Same cross section as for $e+Cl \rightarrow Cl+e$.
[i]Estimated.

$$\frac{1}{\mu_i} = \sum_j \frac{1}{\mu_{ij}}, \tag{14}$$

where μ_{ij} is the mobility of species i in gas j.

The boundary conditions at surfaces for charged species is that they return to the plasma as their neutral counterparts with unity efficiency. The reactive sticking coefficient for the flux of Cl (Cl*) to nonwafer surfaces is 0.005. The reacting atoms return as a flux of 0.5 [Cl_2]. This boundary condition implies that there is a first-order reaction Cl on the surface. The reactive sticking coefficient for Cl (Cl*) on the wafer is 0.05. The reacting atoms return as a flux of 0.25 [$SiCl_4$]. The depletion of Cl_2, and indirectly the electronegativity of the plasma, critically depends on the reassociation coefficient for Cl atoms on the walls, γ.[47,48] Large values of γ result in more rapid replenishment of Cl_2 thereby allowing for dissociative attachment to the molecule. To date, there are no direct measurements of either γ or of fractional dissociation of Cl_2 for the conditions of interest. Our value for γ is an approximation which is supported by data discussed in the following section.

III. VALIDATION

The model was validated by comparing our predicted electron densities with those obtained by microwave interferometry by Greenberg in Ar and Ar/Cl_2 plasmas.[51] The reactor is a Gaseous Electronics Conference (GEC) reference cell[52]

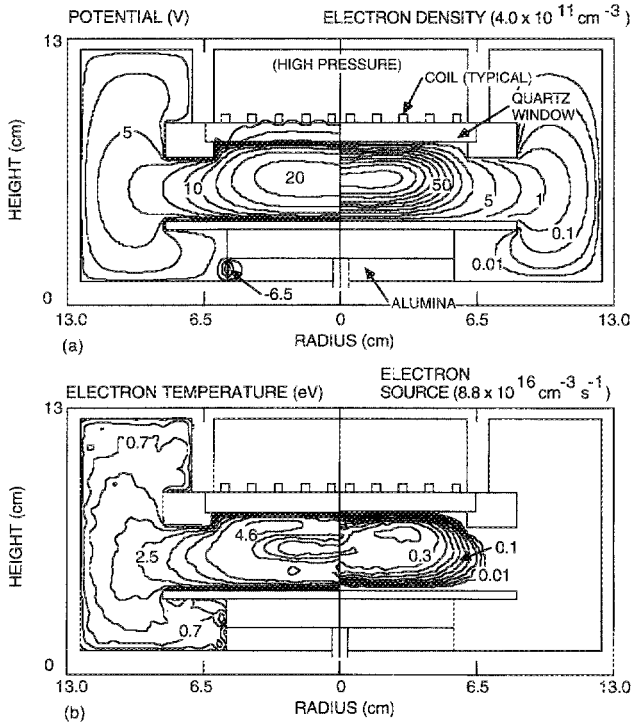

FIG. 3. Computed plasma parameters for the modified GEC reference cell. (a) Time averaged electric potential and electron density and (b) electron temperature and electron source. (The contour labels for the electron density and source are the percentage or fraction of the maximum value shown at the top of the figure.) The gas is Ar at 10 mTorr and the inductive power deposition is 150 W. The electron temperature remains moderately high in the periphery of the reactor.

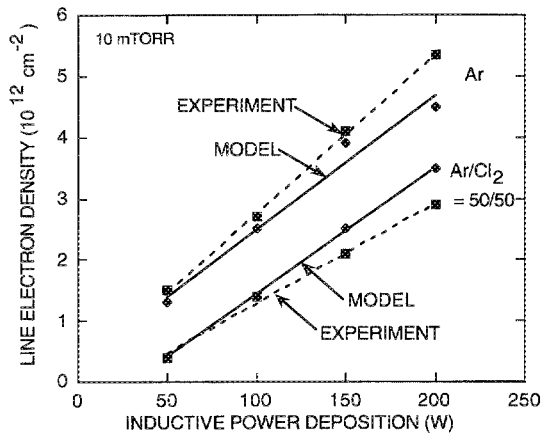

FIG. 4. Comparison of computed and experimentally derived line integrated electron densities as a function of power deposition for Ar and Ar/Cl_2=50/50 gas mixtures in the modified GEC reference cell. The total gas pressure is 10 mTorr. Experimental results are from Greenberg (Ref. 51). The electron density is nearly linearly proportional to power deposition.

which has been modified by removing the capacitively coupled top electrode and replacing it with a dielectric window and coil assembly as shown in Fig. 3. The substrate to window distance is 3.8 cm and the diameter of the substrate is 16.5 cm. The antenna is a five-turn spiral coil spanning the entire diameter of the substrate. Line integrated plasma densities at the axial midplane were measured using a microwave interferometer operating at 80.4 GHz. The experimental results are presented as integrated line densities (cm^{-2}). All measured power depositions were corrected for nonplasma resistive losses. Gas flow rates were typically 10–40 sccm, producing residence times of 0.1–0.5 s.

Typical computed potentials, electron densities, electron source, and electron temperature are shown in Fig. 3 for an Ar plasma. (The electron temperature is defined as $T_e=\frac{2}{3}\langle\epsilon\rangle$, where ϵ is the average electron energy.) The maximum electron density is predicted to be 4.0×10^{11} cm^{-3} with a slight off-axis maximum. The off-axis maximum in plasma density results from the toroidal power deposition which produces an electron (ion) source which is centered at approximately the half-radius 1 cm below the dielectric window, and dominantly produces ions off-axis. The small substrate-to-window separation produces a rapid axial loss of electrons by diffusion thereby preserving the radial distribution of the source function. Note, however, that the plasma appreciably extends beyond the limit of the coils and of the substrates.

The peak electron temperature is 4.6 eV directly below the antenna, where the collisional power deposition and the ion source are maximum. In spite of this component of power deposition being limited to the region directly below the coil, the long mean-free path for electron transport and some component of stochastic electron heating, producing fairly warm electrons throughout the reactor. The plasma potential has a maximum value of 20 V referenced to the grounded substrate and chamber walls. Note the dielectric near the base of the chamber negatively charges to approximately −6 V. The plasma in this region has decayed to a sufficiently low density that the ambipolar electric field is ineffective at balancing the flux of warm electrons (1–2 eV) and positive ions. The dielectric, therefore, charges to a larger negative value (relative to the local plasma potential) than do dielectrics in contact with the bulk plasma where ambipolar diffusion is more effective.

A comparison between our computed line electron densities and those measured experimentally are shown in Fig. 4 for Ar and Ar/Cl_2=50/50 gas mixtures at a pressure of 10 mTorr and inductive power deposition up to 200 W. The agreement between experiment and theory is generally within 20%. For the power and pressure range of the experiments, the plasma densities increase nearly linearly with power deposition and linearly with gas pressure (not shown). The latter trend results from the ion loss being dominated by ambipolar diffusion whose rate is inversely proportional to pressure. These results confirm the collisional nature of the plasma even at these low pressures. Had ion transport been dominantly ambipolar molecular flow as opposed to diffusional flow, the plasma density would not have been a sensitive function of pressure.

Note that the Ar/Cl_2=50/50 gas mixture has an electron density roughly half that of the argon plasma. If the Cl_2 was significantly dissociated (that is, we actually have an Ar/Cl gas mixture), one would expect the plasma density for the Ar/Cl_2 gas mixture to be larger than that for Ar plasma. This expectation results from the facts that momentum transfer

cross section is smaller, ionization threshold is smaller, and ionization cross section is larger for Cl compared to that for Ar. The lower plasma density results from the nonionizing power deposition into Cl_2 (vibrational and electronic excitation, attachment) being large compared to that for Ar. One would, therefore, expect lower plasma densities in Ar/Cl_2 mixtures compared to Ar. (Experimental measurements also showed nearly the same electron density for flow rates of 10–36 sccm. These results imply that Cl_2 is not significantly dissociated since its density does not depend on residence time.) Our good agreement with experiments for plasma density in Ar/Cl_2 gas mixtures provides an indirect validation for our estimation of reassociation coefficient for Cl atoms on the walls.

Experimental[6] measurements of Doppler broadened optical emission from Ar ions suggest that the ion temperature in the bulk plasma exceeds 0.1 eV for the conditions of interest. Computed results for the ion temperature from the PCMCS predict similar temperatures. The ion temperature used for the results just discussed was 0.12 eV. We found that the predicted ion density for Ar plasmas generally increases with increasing ion temperature. (Calculations using room-temperature ions produced plasmas with roughly half the electron densities shown here.) This scaling results from the fact that the mobility of Ar ions decreases with increasing ion temperature for at least $T_I<0.8$ eV.[50] Since the ambipolar diffusion coefficient scales as $\mu_I T_e$, a smaller ion mobility produces lower diffusion loses, which increases the plasma density.

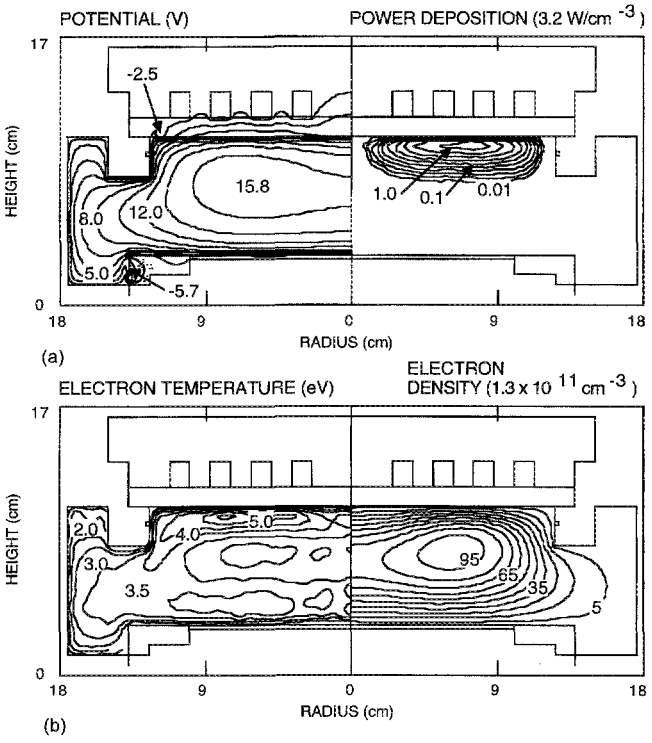

FIG. 5. Computed time averaged plasma parameters for the standard case (Ar/Cl_2=70/30, 5 mTorr, 700 W inductively coupled power). (a) Electrical potential and collisional power deposition. (b) Electron temperature and density. (The contour labels for power deposition and electron density are the fraction or percentage of the maximum value shown at the top of the figure.)

IV. DESIGN ISSUES AFFECTING UNIFORMITY OF ETCHING FLUXES

In this section we will discuss our results from a parametric survey conducted with the model to investigate methods to optimize the uniformity of etching fluxes to the surface of the wafer. The base case for this study uses the geometry shown in Fig. 1, which resembles that of the LAM 9000 series of etching tools. ICP reactors of this type are attractive in that the location of power deposition and uniformity of the ion flux can be controlled by design and placement of the coils; and by the selection of reactor materials. In experimental studies by Patrick *et al.*[7] and Carter *et al.*[8] plasma properties and etching rates were measured for the LAM 9400 reactor. Patrick *et al.* investigated Cl_2 plasmas at 5 mTorr operating with up to 1000 W of inductive power and rf bias powers (applied to the substrate) of up to 100 W. They measured ion densities in the center of 1.8×10^{10}–2.3×10^{11} cm^{-3} for inductive power deposition of 100–950 W, and observed decreasing plasma uniformity with increasing power deposition. Carter *et al.*[8] investigated the effects of inductive power and bias in Cl_2 discharges on SiO_2 and p-Si etch rates. They showed that anisotropic etching occurred primarily at lower pressure and higher rf bias indicating the importance of ion-driven processes, however they concluded that the total etch rate was ultimately limited by the Cl radical concentration.

In the standard reactor, the gas is injected through a ring nozzle pointing radially inward. The nozzle support structure (as well as all other parts unless noted otherwise) is constructed of metal. The pump port, though off-axis in the actual device, is represented by an annular ring in the model. The substrate to window distance is nominally 7.5 cm. The diameter of the quartz window that is exposed to the plasma is ≈24 cm. The 20-cm-diam silicon wafer is surrounded by an annular alumina wafer clamp. The antenna consists of a four-turn coil having square cross section (1 cm×1 cm) which we represented as nested circular coils. Our test system will be etching of p-Si using an Ar/Cl_2 gas mixture at 5 mTorr pressure with a flow rate of 80 sccm and an inductive power deposition of 700 W. The model discussed here does not include surface kinetics algorithms other than those implied by reactive sticking coefficients. We will, therefore, associate etching uniformity with the uniformity of the fluxes of neutral radicals (Cl,Cl*) and ions (Cl^+, Cl_2^+, Ar^+) to the substrate. As we will see below, the neutral radical flux to the wafer is quite uniform compared to that for the ion flux, while the magnitude of the fluxes are commensurate. Under these conditions, the uniformity of the etch will be sensitive to the uniformity of the ion flux.

A. General plasma characteristics and neutral transport

A selection of plasma characteristics for the standard reactor are shown in Figs. 5–7. The advective flow field is shown in Fig. 6. The densities of Cl_2, Cl, Cl , and Cl* are

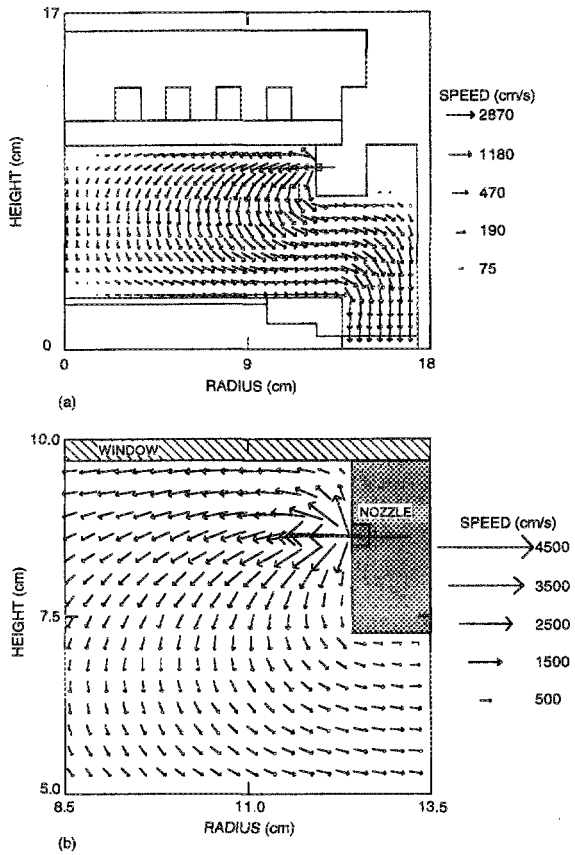

FIG. 6. Computed advective velocity field for the standard case for a total flow rate of 80 sccm and 5 mTorr. The length of the arrows denote the speed. (a) Flow field throughout the reactor scaled over two decades from the maximum. (b) Close-up of flow field near the nozzle using linear scaling. The jetlike input stream penetrates a few centimeters. The central portion of the reactor is nearly advectively stagnant, though it is well mixed by diffusion.

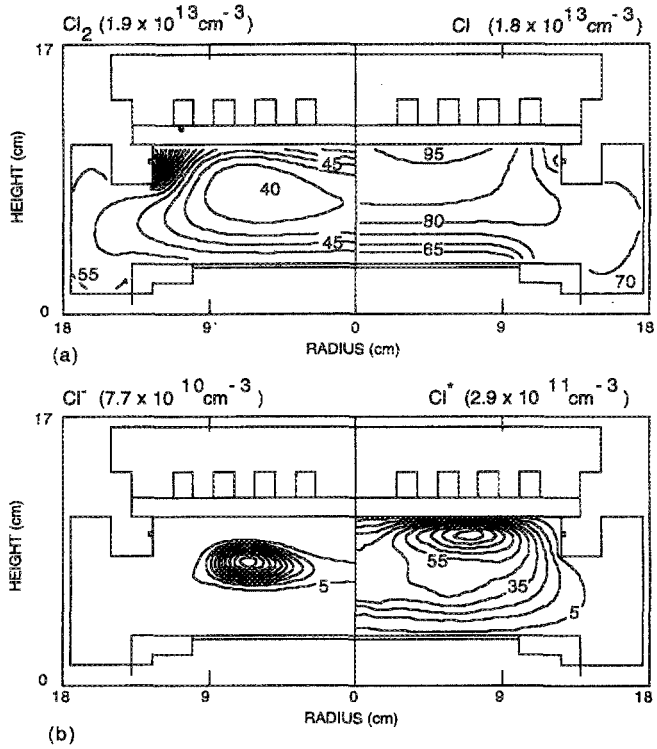

FIG. 7. Computed time averaged chlorine densities for the standard case. (a) Cl_2 and Cl, (b) Cl^- and Cl*. (The contour labels are the percentage of the maximum value shown at the top of the figure.) The maximum Cl_2 density occurs at the inlet while its minimum value is at the center of the plasma where it is depleted by electron impact processes. Cl has local maxima at the walls where it is replenished by quenching or recombination of Cl* and Cl^+. It is depleted at the wafer by the etching reaction.

shown in Fig. 7. The azimuthal electric field, electron/ion source, and Cl_2^+ density are shown in Figs. 8–10 as part of our parametric study for coil placement.

The collisional power deposition (σE^2) is maximum in a toroidal volume centered at approximately half the coil radius. The localized power deposition results from the short skin depth of the electric field. Note that the plotted power deposition in the collisional value as calculated in the EMM and does not include stochastic effects. The stochastic heating of electrons is captured in the EMCS and is reflected in the electron source functions, as discussed below. The electron density has a maximum value of 1.3×10^{11} cm^{-3} with an off-axis maximum, as have the Cl_2^+ and Cl^- densities. The maximum results from both the localized electron source and a shallow local maximum in the plasma potential. The ratio of electron to negative ion density is 1.7:1 at the maximum in the plasma potential where the negative ions "pool." On a reactor averaged basis, however, this ratio is ≈30:1. The negative ion density is a sensitive function of the dissociation fraction of Cl_2, and is discussed in more detail below. The peak plasma potential is 15.8 V. The alumina wafer holder and portions of the quartz window have a net negative potentials. The curvature in the plasma potential is likely overestimated due to the fact that the sheaths are barely resolved by the mesh. The electron temperature has a maximum value of ≈5.5 eV, and remains as high as 2 eV in the peripheries of the chamber. Similar gradients in electron temperature have been observed by Wendt *et al.* for Ar ICPs.[12–15]

A legitimate concern is whether collisional power deposition is a proper description at the low pressures of interest. Stochastic electron heating will play a role at pressures below 10 mTorr as discussed by Turner.[53] In the hybrid model, the calculated collisional power deposition is used to normalize the coil current in the EMM. These fields are used to advance electron trajectories in the EMCS. In this regard, stochastic electron heating is captured in the EMCS and so is reflected in the source functions. Should stochastic heating account for a significant fraction of the power deposition, then the power deposition obtained the EMM would not be totally consistent with that produced in the EMCS. A qualitative measure of the accuracy of our approximations can be obtained by comparing the collisional power deposition shown in Fig. 5(a) with the electron source produced by the EMCS in Fig. 9(a). Power deposition which is dominantly stochastic would likely produce a less localized electron source.

A computed advective flow field is shown in Fig. 6. The jetlike injection of gases from the nozzle extends for only a

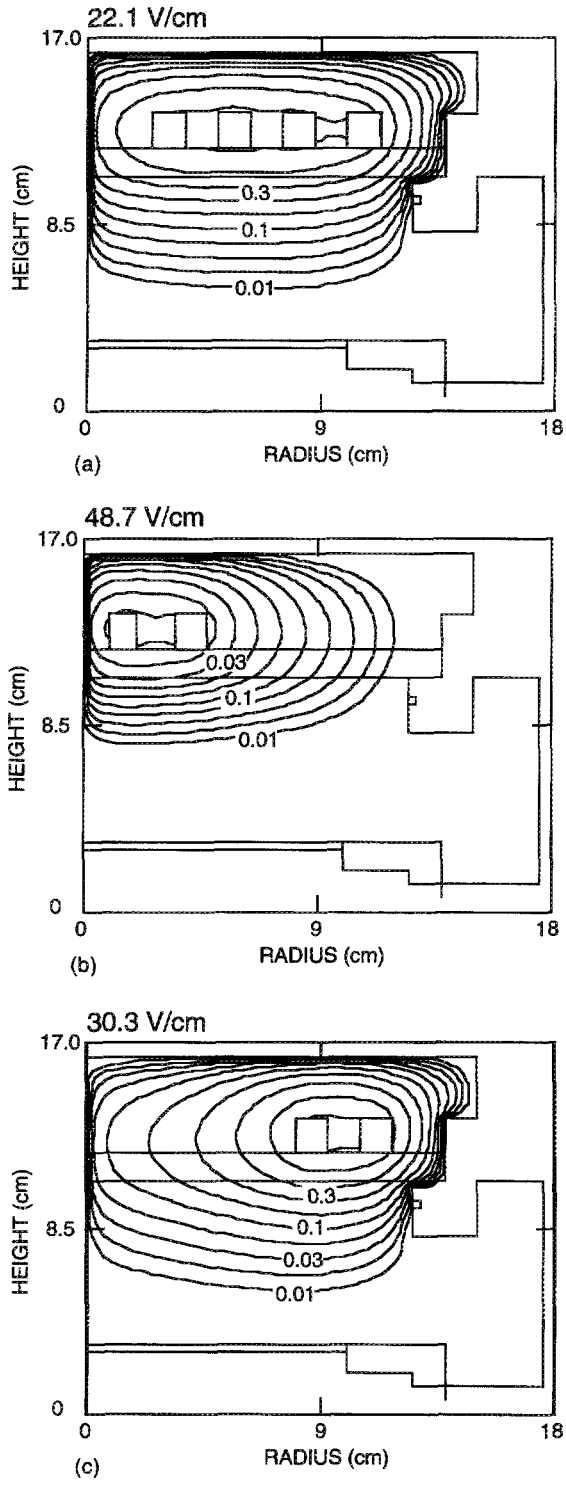

FIG. 8. Amplitude of the azimuthal electric field for the (a) standard, (b) inner, and (c) outer coil configurations. (The contour labels are fractions of the maximum value shown at the top of the figure.) The power deposition is the same for each case, resulting in a higher peak field for the inner coil case; and a lower peak field for the outer coil case.

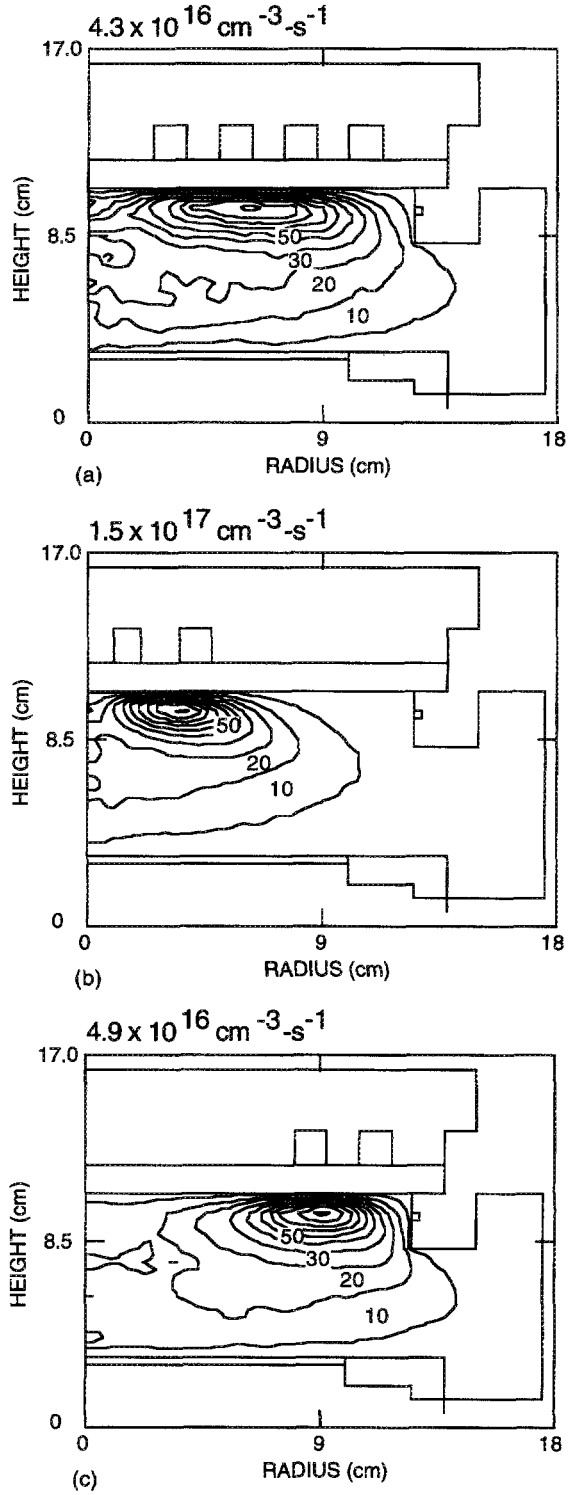

FIG. 9. Electron (total ion) source by electron impact for the (a) standard, (b) inner, and (c) outer coil configurations. (The contour labels are percentages of the maximum value shown at the top of the figure.) The maximum in the electron source occurs within a few centimeters of the quartz window and tracks the peak in the azimuthal electric field.

few centimeters, in agreement with DSMC simulations.[28] The advective speed decreases by a factor of nearly 100 in the center of the reactor compared to the region near the nozzle. In comparison to diffusive speeds, the center of the reactor is advectively stagnant. In the low-pressure systems of interest, the advective gas flow field has a secondary effect on the global plasma properties. As discussed above, the diffusive speeds of molecules greatly exceed the advective ve-

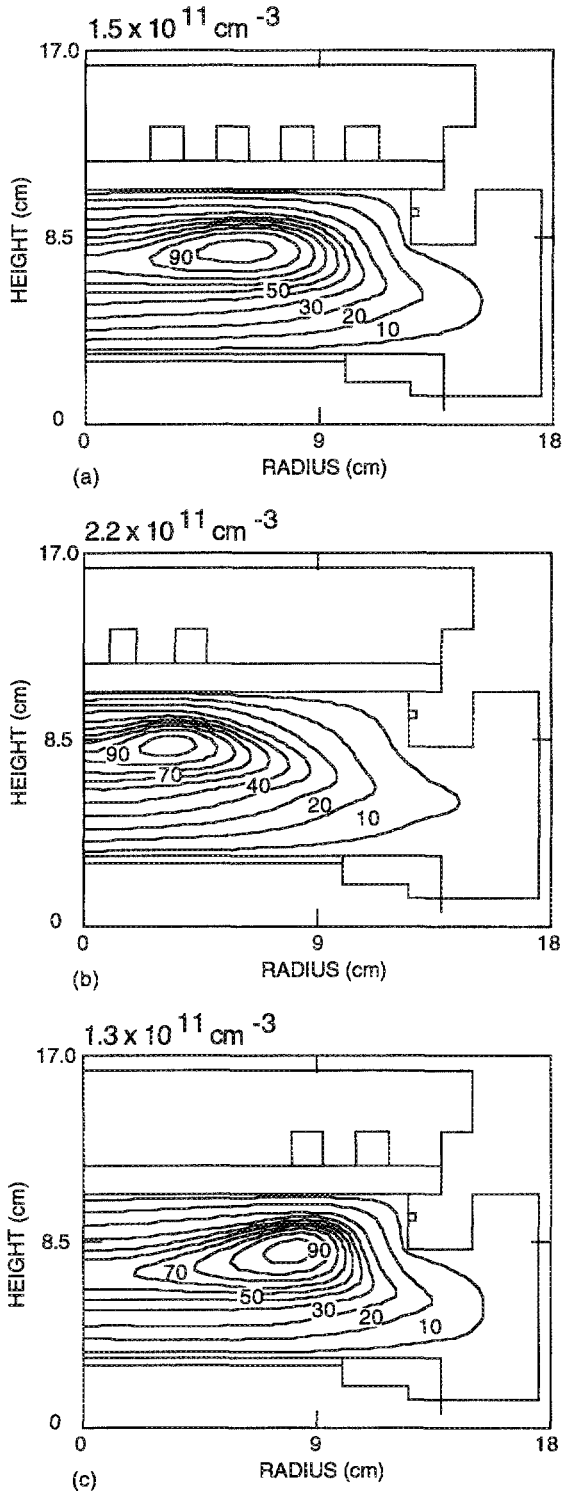

FIG. 10. Cl_2^+ density for the (a) standard, (b) inner, and (c) outer coil configurations. (The contour labels are percentages of the maximum value shown at the top of the figure.) Local extrema in the Cl_2^+ result from the local maximum in the source by electron impact, and from the pooling of Cl^- at the peak of the plasma potential.

locities (except at the nozzle), thereby resulting in the transport of minor species being dominated by diffusion. As a consequence, pressures of less than 10–15 mTorr, the advective flow field is not particularly important in determining the spatial distribution of radicals. The advective flow field does, however, manifest itself by providing local sources of feed stock gases (at the nozzle) and local sinks for products (at the pump port). The details of the balance between gas diffusion and advection are specific to the gas pressure and geometry; and should be considered on a case-by-case basis.

The dominant consequence of gas flow in low-pressure systems is its effect on the average residence time of gases in the reactor and, hence, on the dissociation fraction of the molecular feed stocks. For a given power deposition low residence times result in more energy deposition per molecule and, hence, more dissociation. This is particularly important in molecular gas mixtures where attachment occurs to the molecule but not to the atomic fragments, as is the case for Cl_2. (Electron attachment to Cl is a three-body process which has a negligible rate at the low pressures of interest.) As a consequence, low flow rates (or high power deposition) which result in large amounts of dissociation also produce low negative ion densities. The degree of dissociation of Cl_2 in high plasma density reactors has recently been discussed by Lee *et al.*[47] Dissociation in Ar/Cl_2 reactive ion etching systems has recently been studied by Deskmukh and Economou.[48]

Cl_2 is fragmented by dissociative electronic excitation and by dissociative attachment. If we ignore reassociation reactions or consumption of Cl on surfaces, an estimate of the fractional dissociation of Cl_2 can be estimated from $f_{Cl_2} = k_d n_e \tau$, where k_d is the reactor averaged rate coefficient for dissociation of Cl_2, n_e is the reactor averaged electron density, and τ is the residence time of gas in the reactor. For our conditions, $\tau = 0.18\ (P/F)$s, where P is the pressure (mTorr) and F is the flow rate (sccm). At 5 mTorr and 80 sccm, $\tau = 11$ ms. For a reactor averaged value of $k_d = 5\times10^{-12}$ cm^3 s^{-1}, 0.99 dissociation occurs with $n_e \approx 2\times10^{11}$ cm^{-3}. A 50% dissociation occurs with $n_e \approx 1\times10^{11}$ cm^{-3}. Clearly, in an actual reactor, spatially dependent dissociation rates complicate these issues. It is equally as clear that the typical operating conditions of ICP reactors are in a regime in which small variations in operating parameters, such as power deposition, gas pressure, and flow rate produce large variations in the fractional dissociation of Cl_2, and, hence, in the negative ion density.

The degree to which advection and diffusion influence the spatial distribution of feed stock gases and reaction products is shown in Fig. 7, where the densities of Cl_2, Cl, Cl^-, and Cl* are plotted. These are examples of species which, at the conditions of interest, are feed stock gases consumed by electron impact processes and unreactive on surfaces (Cl_2), products of electron impact which are reactive on certain surfaces (Cl), product of electron impact which are only reactive in the volume (Cl^-), and products of electron impact which are reactive in the volume and deactivated on all surfaces (Cl*). The densities of all products have a local minimum near the input nozzle and by the pump port. Near the nozzle, the high advective velocity and input of fresh gas counteracts diffusion of products generated elsewhere in the reactor. The density of Cl_2 has a local maximum near the input nozzle where the feed stock gas is introduced. The global minimum in the density of Cl_2 occurs in the torus

located 1–2 cm below the dielectric where the power deposition is maximum and where Cl_2 is being consumed by electron impact dissociation. Cl has a local maximum in the same region since the dissociation of Cl_2 produces a source of Cl. The global minimum in Cl atom density occurs at the surface of the wafer where the etching reaction consumes Cl. Note that Cl_2 has small local maxima at the walls due to reassociation of Cl atoms which produces a source there. Cl also has small local maxima at the (nonwafer) surfaces due to a source resulting from deactivation of Cl* and recombination of Cl^+. The latter contribution is commonly called "ion pumping" in which atoms are ionized and rapidly transported to the walls by ambipolar diffusion. Cl* has a large density only near the source since it has a relatively short radiative lifetime and is deactivated on all surfaces. We compared results from the model between cases which used the advective flow field and cases which accounted for flow using average residence times. With the exception of the region close to the nozzle (increase in densities of feed stock gases, decrease in densities of products) the resulting densities and fluxes were little changed.

B. Coil placement

Coil placement, above all other design variables, most directly affects plasma uniformity. Modeling results by Paranjpe,[20] and experiments by Barnes[54] and Fukasawa *et al.*[16] have demonstrated the ability to engineer the spatial distribution of the plasma by coil placement. This issue was also addressed by Coultas and Keller in a patent disclosure.[55] Due to the short skin depth (1–2 cm) for the systems of interest, power deposition occurs dominantly in the proximity of the coils, a condition which is exacerbated by fact that collisional power deposition scales as σE_θ^2. The location of electron impact events having high thresholds such as ionization can, therefore, be controlled by carefully selecting the coil layout. Ultimately, at low power and high plasma conductivity the distribution of power deposition will be limited by skin depth considerations.

To demonstrate the control over ionization rates afforded by coil placement, we have parametrized our model using standard, inner, and outer coil configurations. The standard coil configuration has four equally spaced turns spanning the radius of the wafer. The inner coil configuration retains only the two first turns of the standard coil, while the outer coil configuration retains on the outer two turns of the standard coil. The azimuthal electric field E_θ, electron source, and Cl_2^+ ion densities for these three cases are shown in Figs. 8, 9, and 10, respectively. The axial fluxes of Cl_2^+ to the wafer for all geometries are shown in Fig. 11. In our particular geometry, symmetry requires that the azimuthal electric field be zero on the axis, while skin depth considerations cause the electric field to functionally be zero on the exterior chamber walls. In the standard geometry, the electric field is maximum at approximately half the radius, and produces power deposition and ionization sources in a torus centered at approximately half the radius 1–2 cm below the dielectric. The maximum value of E_θ in the plasma portion of the reactor is ≈8 V/cm at the dielectric. The local source of Cl_2^+ produces a local extrema in its density at that location. (In the standard

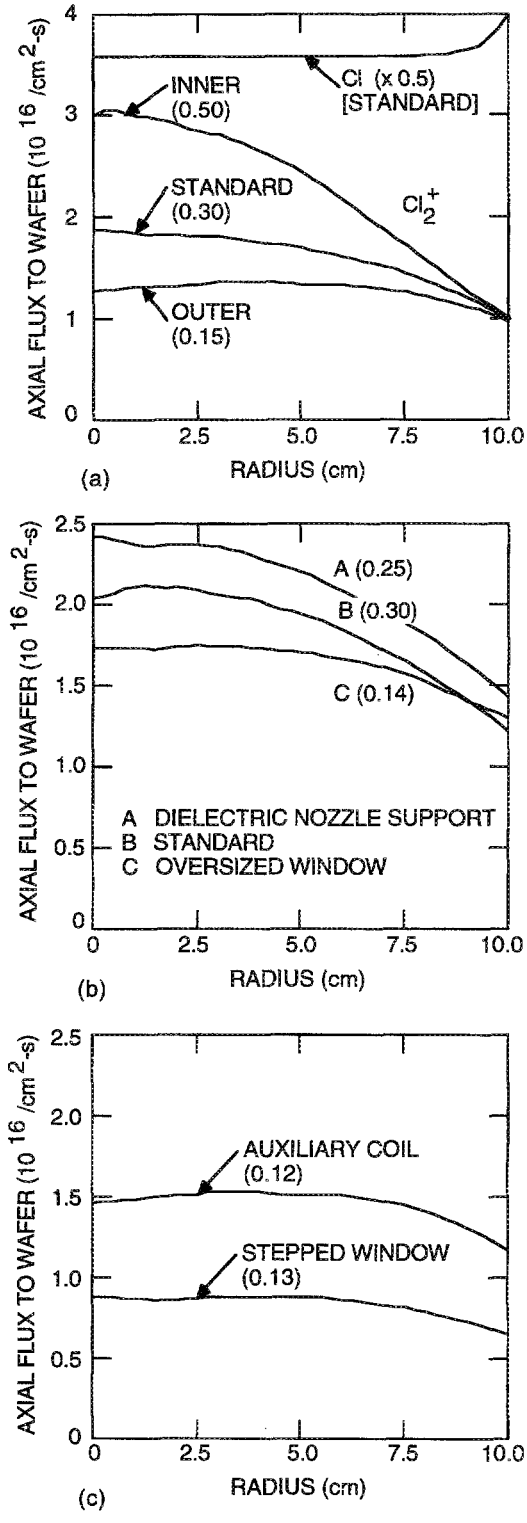

FIG. 11. Axial flux of Cl_2^+ incident onto the wafer. (a) Fluxes for the standard, inner, and outer coil configurations. The flux of Cl is also shown. (b) Fluxes when using the dielectric nozzle support, standard case and the oversized window. (c) Fluxes for the designs using the auxiliary coil and stepped window. The numbers in parentheses by each label are the uniformity parameters, η.

case, the Cl_2^+ density is approximately equal to but usually larger than the Ar^+ density; and approximately twice the Cl^+ density.) The local peak in Cl_2^+ density results, in part, from pooling of Cl^- at the maximum in the plasma potential,

which occurs near the peak of the ion source. In the Ar/Cl_2 system the degree of "pooling" of negative ions critically depends on the fractional dissociation of Cl_2. Diffusion ultimately homogenizes the ion flux to the substrate thereby producing a more uniform radial profile, as shown in Fig. 11(a). For purposes of comparison, we define the uniformity of the ion flux η as (max−min)(max+min). η has a range of (0,1) with smaller values being more uniform. For the standard case, η=0.31.

Placing the coils at small radii produces an electric field and ion sources having maxima at smaller radii. Since the total power deposition is being held constant, the maximum electric field, ion sources, and ion density (all located at small radii) are larger since the incremental volume element is smaller. As the ions diffuse to larger radii (where the ion source is small) the ion flux necessarily decreases since the total fluence (flux×area) is at best conserved. In reality the fluence decreases because there are losses of Cl_2^+ by diffusion to the upper and lower surfaces. This results in a centrally peaked, nonuniform ion flux to the wafer (η=0.50), as shown in Fig. 11(b).

Placing the coils at large radii produces an electric field and ion source with maxima at larger radii. Since, again, the total power deposition has been held constant, the electric field, ion source and ion density have peak values which are smaller than the standard case due to the larger incremental volume. The ions now diffuse from the ionization source at large radii to smaller radii. This results in a converging flux which compensates for losses to the upper and lower surfaces. The end result is a more uniform plasma and a fairly uniform flux of ions to the wafer (η=0.15), as shown in Fig. 11(c). These results corroborate experiments performed by Fusakawa *et al.*[16] in which a single turn coil at a large radius produced a more uniform plasma than a multiturn coil spanning the radius.

Note that in all cases, the fluxes of Cl atoms to the wafer are quite uniform compared to the ion flux as shown in Fig. 11(a). This results from Cl atoms having a low reactive sticking coefficient on nonwafer surfaces thereby producing a Cl density which is nearly uniform as a function of position. In particular, the Cl has a low reactive sticking coefficient on the wafer holder and a large reactive sticking coefficient on the wafer. The Cl flux to the wafer has a small maximum near the edge and minimum near the center. This results from the flux of Cl atoms being "supplied" from large radii and being "consumed" at small radii.

The scaling we have discussed here, placing ion sources at larger radii, succeeds because the diffusion lengths of ions are geometrically and not kinetically constrained. For these conditions the loss of electrons and ions are dominanted by recombination at the walls. At higher pressures or in more electronegative gas mixtures, volumetric losses of electrons and ions by recombination or ion–ion neutralization dominate. In those cases diffusion lengths are determined by the kinetic mean-free path for volumetric loss. Coil configurations which place sources at large radii will produce ion fluxes which are highest at large radii. Under those conditions, uniform ion fluxes can only be obtained by having uniform ion sources.

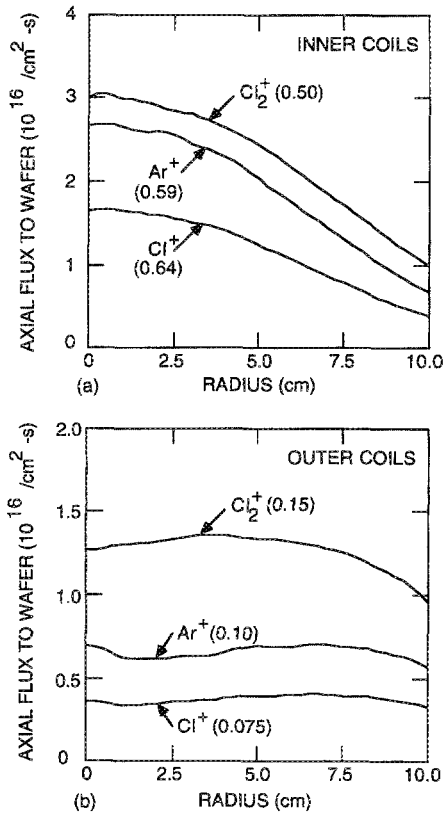

FIG. 12. Axial flux of Ar^+, Cl^+, and Cl_2^+ for the (a) inner and (b) outer coil configurations. The numbers in parentheses by each label are the uniformity parameters, η. The coil geometry not only influences the uniformity of the flux but also the relative magnitudes of the flux of different ions. This results from the change in the relative proximity of the ion sources from the wafer and charge exchange collisions which occur during transport to the wafer.

The placement of the coils not only affects the uniformity of the ion flux but can also affect the relative compositions of the ion flux to the substrate. This is demonstrated in Fig. 12, where the fluxes of Ar^+, Cl^+, and Cl_2^+ to the wafer are shown as a function of radius for the inner and outer coil cases. The uniformities of the Ar^+, Cl^+, and Cl_2^+ fluxes with the inner coils are η=0.59, 0.64, and 0.50. For the outer coils, the uniformities are η=0.10, 0.075, and 0.15. The improvement in uniformity when using the outer coils is greatest for Cl^+ and worst for Cl_2^+. With the inner coils the proportions of ions which are Ar^+ and Cl^+ are larger relative to Cl_2^+ compared to the case with the outer coils. For example, with the inner coils, the ratio of ion fluxes to the wafer are Ar^+/Cl_2^+=0.88 and Cl^+/Cl_2^+=0.54. For the case with outer coils the flux ratios are Ar^+/Cl_2^+=0.52 and Cl^+/Cl_2^+=0.29. When the coils have large radii, the ion sources are, on the average, physically further from the wafer than when using inner coils. Therefore, with the outer coils, ions produced by electron impact have more opportunity to undergo charge exchange reactions before arriving at the wafer. As a result, the flux of ions contains a larger proportion of charge exchange products. In our reaction scheme Cl_2^+ is produced by direct electron impact of Cl_2 and by charge exchange from Ar^+ and Cl^+ to Cl_2. Cl^+ is produced by electron impact of

Cl and charge exchange of Ar^+ with Cl. Ar^+ is produced primarily by electron impact excitation of Ar and is lost by charge exchange to Cl and Cl_2. As a consequence, Ar^+ and Cl^+ ions which are produced at large radii will be depleted relative to Cl_2^+ when arriving at the wafer due to charge exchange processes.

C. Reactor materials

The choice of reactor materials plays an important role in the spatial distribution of power deposition and ultimately on the ion flux to the substrate. In the cases just discussed, the coils are located interior to the metal structure supporting the gas injection nozzles and windows. This configuration confines E_θ to radii smaller than the support structure due to the fact that E_θ must be zero on its surface. Since the power deposition scales as σE_θ^2 (the plasma conductivity also decreases approaching the structure), there is a substantial decrease in power deposition at large radii. This condition can be remedied, and the uniformity of the ion flux improved, by moving these metal structures to larger radii or replacing them with ceramics. The ceramic materials allows penetration of the electric field, thereby increasing E_θ in the plasma near the surface.

This change in design is demonstrated in Fig. 13, where E_θ, the electron source, and the Cl_2^+ density are plotted in a reactor in which the metal nozzle support structure is replaced by one made of alumina. Note that E_θ penetrates into the ceramic, however, it is ultimately constrained by both the metal (grounded) nozzle and the metal support structure above the ceramic. The end result is that the electric field is moderately larger at larger radii but produces only a small increase in power deposition and electron source at large radii. The desired goal of increasing the ion flux at large radius relative to the standard case is only moderately met, as shown in Fig. 11(b). The uniformity of the ion flux is only slightly improved (η=0.25) compared to the standard case. This result emphasizes the importance of the design of the ICP chamber external to the plasma as well as of the chamber in contact with the plasma with respect to tailoring power deposition to obtain the desired flux profiles to the wafer.

For the test conditions, improving the uniformity of the ion flux incident onto the wafer requires moving ion sources to large radii, if not exclusively than to improve the uniformity of the ion source. This goal may be difficult to achieve when the electric field is confined by the window support structure. An alternate strategy is to oversize the window and coil to place the edge of the wafer beneath the region of high power deposition and large ion source. This strategy is embodied in the second design shown in Fig. 13. Here the window has a larger diameter, an additional turn is added to the coil and the support structure for the nozzle is dielectric. The maximum in the azimuthal electric field and the electron source is now located at approximately the edge of the wafer, which appears to be nearly ideal placement for these conditions. The maximum in the Cl_2^+ density shifts to larger radii and the ion flux to the substrate is markedly more uniform, as shown in Fig. 11(b) (η=0.14). However, since the total power deposition has been held constant, while the volume of the plasma has increased, the magnitude of the ion flux

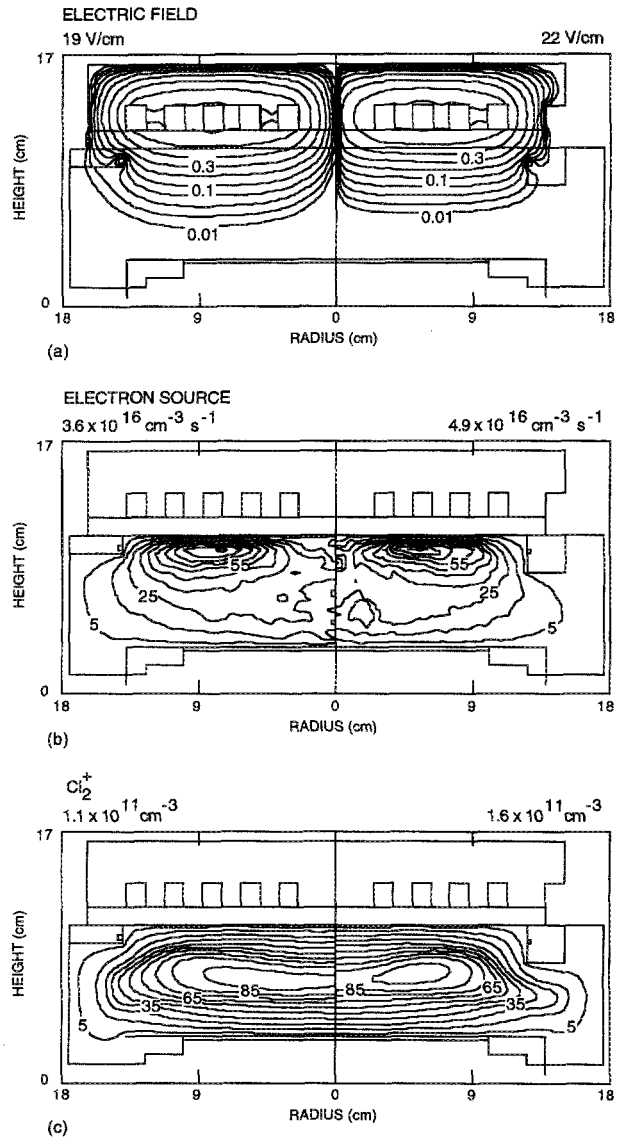

FIG. 13. Plasma parameters for reactor designs employing an oversized window and coil (left column); and a dielectric nozzle holder (right column). (a) Electric field, (b) electron (total ion) source, and (c) Cl_2^+ density. (The contour labels are percentages or fractions of the maximum value shown at the top of the figure.) The case with the dielectric nozzle holder produces only moderately more uniform conditions compared to the standard case due to the confinement of the azimuthal electric field by the metal reactor materials. The design having an oversized window produces noticeably more uniform fluxes.

decreases. We, therefore, have a design tradeoff between uniformity and magnitude of the flux for a given power.

A different design which increases the ion source at large radii uses an auxiliary single turn solenoid in addition to the stove-top coil. In principle, the stove top and solenoid can be separately powered and have different frequencies. This design appears in Fig. 14 where the electric field, electron/ion source and Cl_2^+ density are shown. The single turn solenoid serves to increase the electric field, power deposition, and ion source at large radii relative to the standard case, while the stove-top coil maintains the ion flux at small radii. The uniformity of the ion flux to the wafer is significantly im-

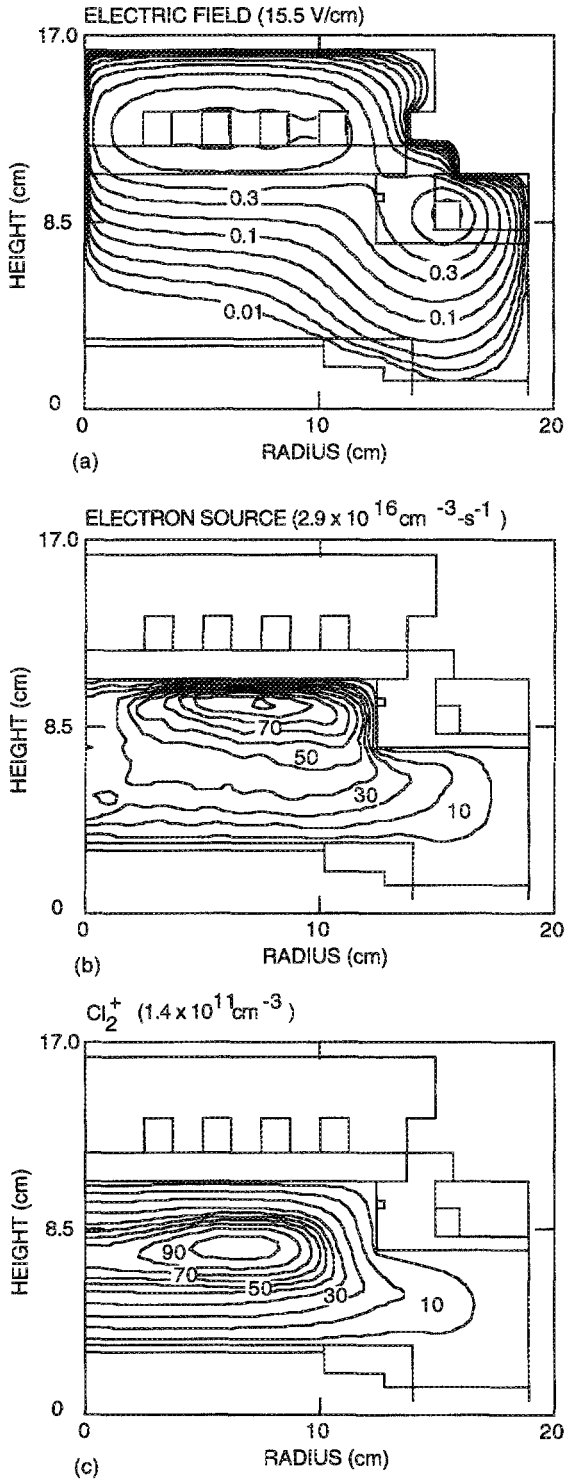

FIG. 14. Plasma parameters for the reactor design employing an auxiliary coil and dielectric nozzle holder. (a) Amplitude of the azimuthal electric field, (b) electron (total ion) source, (c) Cl_2^+ density. (The contour labels are percentages or fractions of the maximum value shown at the top of the figure.) The auxiliary coil increases the electric field and source at large radii, thereby producing more uniform fluxes to the substrate.

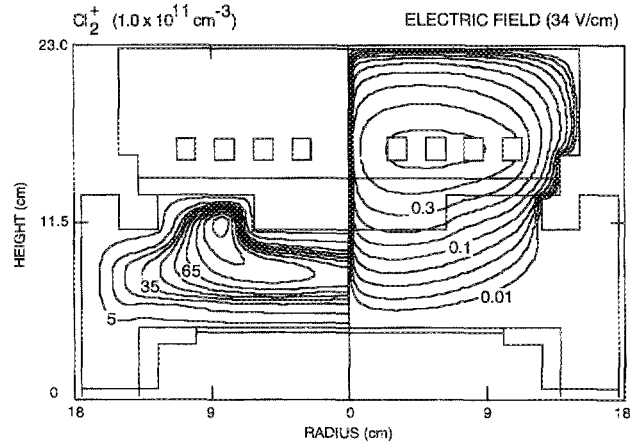

FIG. 15. Plasma parameters for a reactor using a stepped window. (a) Cl_2^+ density and (b) amplitude of the azimuthal electric field. (The contour labels are percentages or fractions of the maximum value shown at the top of the figure.) Using a stepped window (thin at large radii) improves the coupling of the electric field to the plasma, thereby producing high plasma densities at large radii.

proved (η=0.12) compared to the standard case, as shown in Fig. 11(c). The uniformity of the ion flux can be fine tuned by adjusting the relative currents between the solenoid and the stove-top coil. In doing so, one can shift the radius at which the maximum in the electron source appears without making mechanical changes to the chamber. One could conceivably "raster" the maximum in the ion source between small and large radii during the etch process by changing the relative currents between the solenoid and stove-top coil to smooth local nonuniformities in the ion flux.

One can obtain a similar increase of the electron and ion source at large radii by thinning the dielectric at large radii thereby enabling more penetration of the electric field and higher power deposition at those locations. This strategy, first suggested by Schlosser[56] and Paranjpe,[20] is implemented in Fig. 15. The window is stepped to a smaller thickness at large radius. The electric field and ion source increase at that location, producing a larger ion density. The ion flux is proportionally more uniform (η=0.13), as shown in Fig. 11(c), though at the cost of reducing the magnitude of the flux.

The etch rate of p-Si is clearly a function of both the neutral Cl flux and the ion flux. In our simulations, the Cl flux is radially fairly uniform while the radial ion flux considerably varies. Experimental validation of the trends we have just discussed may be inferred from etching rates of p-Si as a function of radius in ICP reactors which embody some of these design features.[54] These etching rates, provided by M. Barnes of LAM Research, are shown in Fig. 16 for similar conditions to the standard coil design, coils placed at large radii and using a stepped window. For purposes of comparison, we have replotted the Cl_2^+ ion fluxes for these cases in Fig. 16(a) normalized to unity to emphasize profile over magnitude. The etch rates have been similarly normalized. The etch rate using the standard coil configuration is least uniform as a function of radius. The uniformity improves when using the stepped window and the outer coils. These results qualitatively agree with the design studies just discussed, and indicate contributions of both the Cl and ion fluxes to the etch rate.

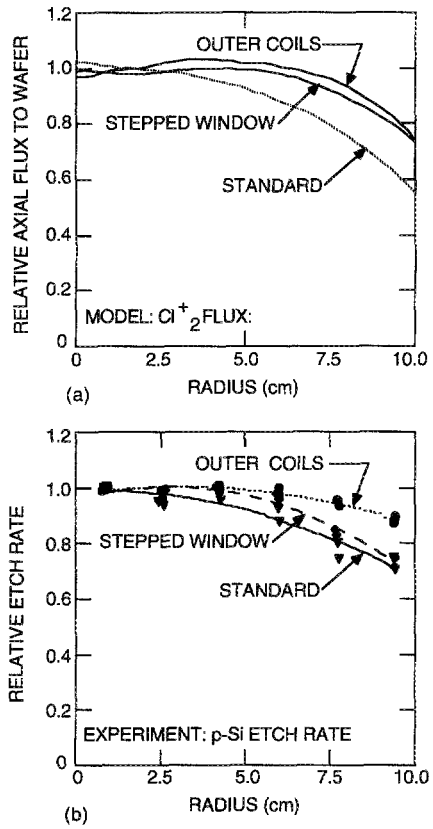

FIG. 16. Comparison of computed ion fluxes and experimental etch rates. (a) Normalized axial Cl_2^+ flux to the wafer for the standard, outer coils and stepped window configurations. (b) Normalized etch rate for p-Si for reactors using similar designs. The experimental data were provided by M. Barnes (Ref. 54). The improved uniformity of the ion flux correlates with improved etching uniformity.

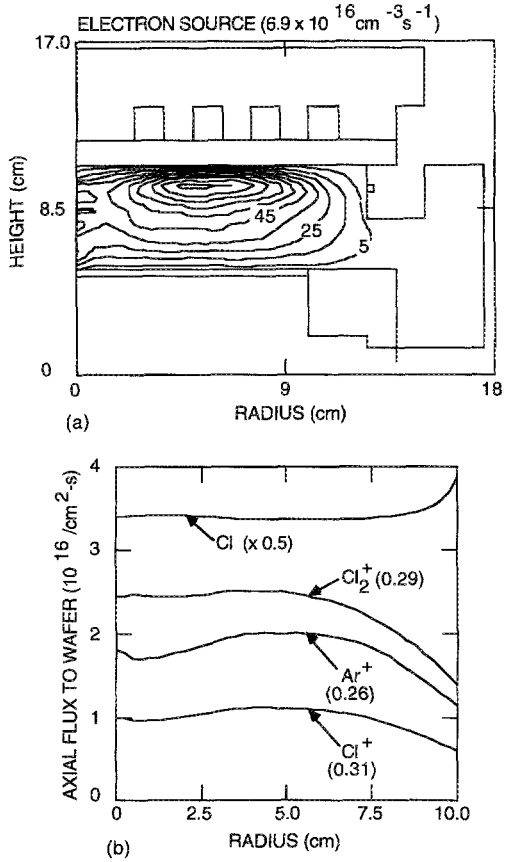

FIG. 17. Plasma parameters for a reactor having a small aspect ratio (5-cm wafer-to-window distance). (a) Electron source (the contour labels are percentages of the maximum value shown at the top of the figure); and (b) axial precursor fluxes to the wafer. The numbers in parentheses by each label are the uniformity parameters, η. The closer proximity of the electron and ion source to the wafer increases the ion fluxes at intermediate radii.

D. Aspect ratio

The reactor aspect ratio (plasma height divided by radius) can have an important effect on ion uniformity to the substrate when the ion source is not uniform. When the ion losses are dominated by recombination at the wall, the ion sources are located far from the wafer and the aspect ratio of the reactor is near unity, diffusion has ample opportunity to assume its fundamental mode. The end result is that the flux is maximum at the center of the wafer. As the aspect ratio decreases and the ion source approaches the wafer, the ion flux to the wafer more closely mirrors the ion source. At intermediate aspect ratios, lowering the ion source towards the wafer has the effect of increasing the ion flux at large radii relative to the center and, therefore, can result in a more uniform flux. At small aspect ratios, diffusion is not able to homogenize the ion flux, and so the ion flux to the wafer will mirror the ion source.

As a demonstration of the importance of aspect ratio in reactor design the ion source and precursor fluxes to the wafer are shown in Fig. 17 for a low aspect ratio reactor. (The wafer to window distance is 5 cm.) The conditions are otherwise the same as for the standard case. The low aspect ratio reactor has only a slightly smaller electron density and higher electron source than the standard reactor since the diffusion losses to the axial surfaces are greater. The spatial distribution of the electron source is little changed from the standard cases since the skin depth in either reactor is less than the substrate-to-window distance. The ion fluxes to the wafer, as measured by η, are not significantly different from the standard case. However, the radial distribution of the ion fluxes are flatter and qualitatively better than the standard case. This results from the ion source being physically closer to the wafer. The ion flux is, therefore, raised at intermediate radii thereby flattening the distribution. (This is particularly apparent in the Ar^+ and Cl^+ fluxes.) The optimum placement of the coils clearly depends on the aspect ratio of the reactor. Smaller aspect ratios require more uniform ion sources since diffusion is less effective at homogenizing the ion flux.

E. Power deposition

Power deposition also plays a role, though somewhat less important, in determining the uniformity of ion flux to the wafer. Langmuir probe measurements by Patrick *et al.*[7] showed that the uniformity of the plasma in the LAM 9400 reactor decreased with increasing power deposition, corroborating visual observations made in other reactors. The details of the uniformity of the plasma and ion flux on power depo-

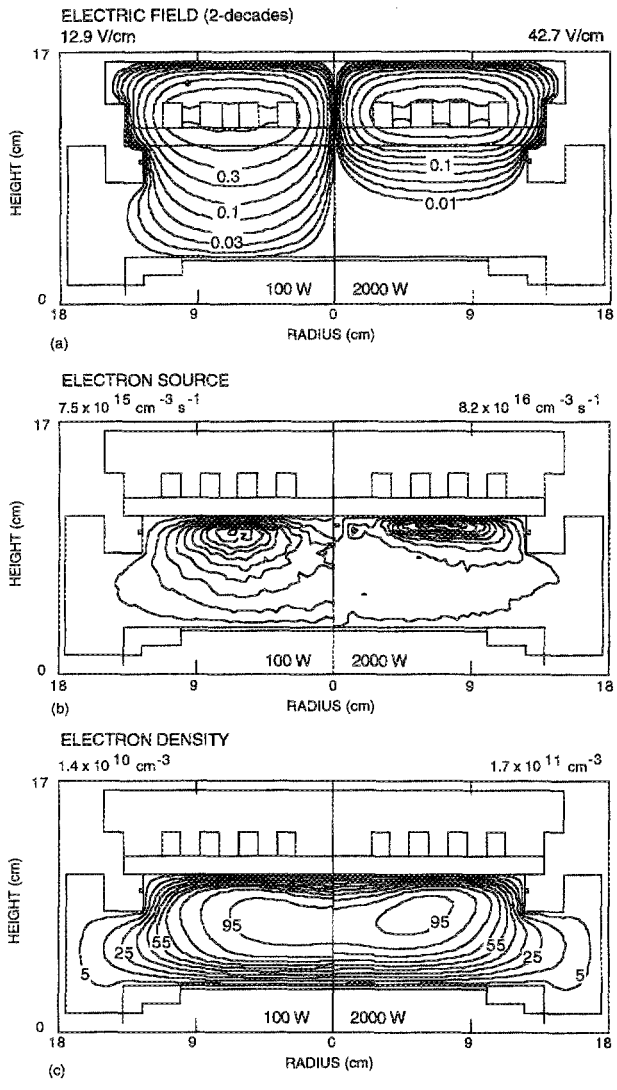

FIG. 18. Plasma parameters for the standard configuration operated at inductive powers of 100 W (left column) and 2000 W (right column). (a) Amplitude of the azimuthal electric field, (b) electron source, and (c) electron density. (The contour labels are percentages or fractions of the maximum value shown at the top of the figure.) The larger skin depth of the low power case results in more uniform excitation of the plasma.

sition do, of course, depend on the details of the geometry but, in general, can be explained by the finite skin depth of the plasma.

For the purposes of this discussion we will use the standard geometry having a four-turn stove-top coil. The azimuthal electric field, electron source, and electron density are shown in Fig. 18 for power depositions of 100 and 2000 W. The peak electron densities are 1.4×10^{10} and 1.7×10^{11} cm^{-3}, respectively. At the lower power deposition, the plasma density is lower and the skin depth is longer. The electric field, therefore, penetrates further into the plasma. This results in a more uniform, though smaller, electron source which ultimately produces a fairly uniform plasma density. At the higher power, the skin depth is proportionally smaller, resulting in electron and ion sources which are dominantly confined to thin region adjacent to the window. In this design, the contours of the electric field have curvature as they enter the plasma. (This curvature is, in part, responsible for the toroidal power deposition.) At high power, and small skin depths, the curvature tends to localize the electron source to a smaller radial extent. The diverging ion flux emanating from the local ion sources produces a less uniform flux to the wafer.

F. dc bias

When an rf bias is applied to the substrate of the ICP reactor, the asymmetry of the resulting capacitively coupled discharge produces a dc bias. The behavior of the dc bias in ICP reactors has been the subject of a number of recent investigations, among them Patrick *et al.*,[7] Fusakawa *et al.*,[16] and Ra and Chen.[57] These workers have found that the dc self-bias is a function of both the inductively and capacitively coupled rf power. An ICP reactor having an rf bias on the substrate is functionally a capacitively coupled reactive ion etching discharge with an external source of ionization provided by the inductively coupled power. The "grounded" electrode opposing the powered RIE electrode is somewhat ill defined. Conduction current flows to ground through any metal surfaces exposed to the plasma (e.g., chamber walls, injection nozzles). Displacement current additionally flows to ground through the dielectric window, or dielectric covered metal surfaces in contact with the plasma. Not unexpectedly, we have found that the dc bias on the substrate depends on the electrical characteristics of materials interfacing with the plasma. In this regard another design parameter is the degree to which materials in contact with the plasma affect the dc bias on the powered electrode; and the degree to which the dc bias can be controlled by the choice of construction materials.

Recall that a dc bias on the powered electrode results from the differences in sheath voltage which results from the necessity to draw equal currents on either electrode averaged over the rf cycle. Conducting surfaces may support a higher rms current (conduction and displacement) than do dielectric surfaces (displacement current only), and thin dielectrics having large permittivities may support more displacement current than do thick dielectrics having small permittivities. Therefore, strategic placement of dielectric liners over metal surfaces in contact with the plasma will produce different, and perhaps controllable, dc biases for the same rf applied voltage.

To illustrate these points, we applied a 75-V amplitude (13.56-MHz) bias to the substrate of an ICP sustained in a 5-mTorr, $Ar/Cl_2=70/30$ mixture. The ICP power is 700 W while the capacitively coupled power from the rf bias is $\approx$100 W. Capacitive coupling resulting from the inductive voltage drop across the coil was also included. The coil was grounded at the center and powered at the outer turn. The voltage was graded across the turns of the coil (0–200 V) and was 180° out of phase with the voltage applied to the substrate.

The plasma potentials averaged over an rf cycle (at $r=0$) are shown in Fig. 19 for reactors having a conducting wafer. Results are shown for the nozzle support structure being either metal or dielectric. The wafer, wafer holder, and sub-

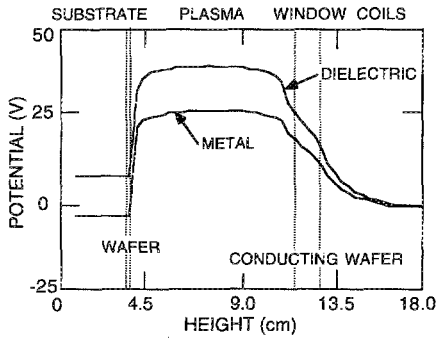

FIG. 19. Time averaged plasma potential ($r=0$) for 700-W inductive power deposition and 100-W rf bias on the substrate (75-V amplitude) when using an electrically conducting wafer. Results are shown for the nozzle support being either dielectric or metal. The dc bias on the substrate is more negative when the nozzle support is metal. The metal nozzle holder collects more current, thereby increasing its "electrical area."

strate are on the powered side of the rf bias circuit. All other surfaces are on the grounded side of the rf bias circuit. The majority of the area of the grounded electrode that is in contact with the plasma is covered by dielectric. The grounded metal walls of the chamber are far from the bulk plasma and collect little current. The displacement current density to the dielectric covered grounded electrode is smaller than the conduction and displacement current density to the wafer. Therefore, in spite of the fact that the geometrical surface area on the grounded side of the circuit is larger than on the powered side of the circuit, the "electrical area" (defined by $\int j \cdot dA$ in the absence of a bias) of the grounded side is smaller than the powered side. The dc bias on the substrate is, therefore, positive and in this case $\approx$10 V. When the nozzle support structure is metal, the electrical area of the grounded side of the circuit increases and exceeds that of the powered electrode. This results from the fact that the sum of the conduction and displacement current to the grounded nozzle support structure exceeds the displacement current when it is a dielectric. The end result is that the dc bias on the substrate becomes negative (≈ -3 V).

It has been experimentally observed[7,16,57] that when ICP reactors are operated at high inductive powers and low rf biases on the substrate, the dc self-bias on the substrate is small (negative) or may be positive. For the identical reactors and gas mixtures, the dc bias is negative for large rf biases or low ICP power. At high inductive powers the plasma density is high and charged particle fluxes are dominated by ambipolar currents to the reactor walls and substrate which, by definition, must sum to zero. The perturbation to the large ambipolar currents produced by an rf bias is small and so the dc bias is small. At low ICP power the fraction of the charge particle flux which can be attributed to the rf current is proportionally larger, and so the magnitude of the dc bias is larger. When operating with a higher ICP power, the plasma density is higher, the sheaths are thinner and so the capacitance of the sheaths are larger. The increased capacitance of the sheaths may also contribute to the lower dc bias.

To demonstrate these points, we have applied a 75-V (amplitude) rf bias to the standard reactor having a conductor wafer with 100 and 1000 W of inductively coupled power. The dc bias for the case with the low ICP power is -35 V, while the dc bias for the case with high ICP power is nearly zero. The evolution of dc biases in ICP reactors will be discussed in more detail in a future publication.

V. CONCLUDING REMARKS

A 2D hybrid model for ICP etching reactors has been used to investigate methods to optimize the uniformity of etching precursors to the wafer for Ar/Cl_2 gas mixtures at powers and flow rates at which the chlorine is not totally dissociated. Particular attention has been paid to the influence of coil design on the uniformity of the plasma sources and subsequent ion flux. We have shown that at a pressure of 5 mTorr, moving the ion sources to larger radii near the edge of the wafer results in more uniform ion fluxes to the wafer. This may be accomplished by either removing ion sources (removing coils) at small radii or adding ion sources (adding coils) at large radii. In all cases, the flux of Cl atoms is uniform compared to the ion flux due to the low reactive sticking coefficient of Cl on nonwafer surfaces. Increasing coil power in general produces less uniform ion fluxes due to having more localized ion sources. Low aspect ratio reactors may produce less uniform ion fluxes since the ion sources are physically closer to the wafer, thereby producing a flux which mirrors the source. However, the optimum aspect ratio is a function of the coil design and placement (in radius) of the sources, as well as pressure. The placement of metal structures within the chamber or adjacent to the coils confines the azimuthal electric field producing sources which are lower near those surfaces. An optimum design strategy would move metal structures beyond the diameter of the wafer and oversize the coil to insure that the plasma source extends to its edge. For the conditions of this study, the advective gas flow patterns play little role in the uniformity of the plasma since diffusion quickly volume averages the source and sinks of gases at the nozzle and pump ports. The role of advection is a sensitive function of pressure and geometry.

We also found that the materials in contact with the plasma acutely affect the dc bias on the substrate. When an rf bias is applied to the substrate, the ICP functionally operates as an RIE discharge. The dc bias is determined by the relative currents collected by the powered and "grounded" sides of the bias circuit. Dielectric covered metal surfaces generally collect different current than do the bare metal surfaces. The dc bias can, therefore, be controlled by appropriate choice of materials.

ACKNOWLEDGMENTS

The authors would like to thank M. Barnes, D. Schlosser, N. Benjamin, R. Van Muers, P. Miller, K. Greenberg, A. Wendt, and M. Hartig for discussions on the design of ICP etching equipment. The authors would like to particularly thank M. Barnes and K. Greenberg for sharing their experimental data prior to publication. The authors also would like to thank D. Economou for sharing his chlorine reaction da-

tabase with us. This work was supported by Sandia National Laboratory/Sematech, LAM Research, Semiconductor Research Corp., the National Science Foundation (ECS91-09362 and CTS91-13215), and the University of Wisconsin ERC for Plasma Aided Manufacturing. We acknowledge the technical assistance of J. Barich who was supported by the NSF Research Experiences for Undergraduates Program.

[1]J. Hopwood, Plasma Sources Sci. Technol. **1**, 109 (1992).
[2]Solid State Technol. **36**, 30 (1993).
[3]J. Keller, M. S. Barnes, and J. C. Forster, in Proceedings of the 42nd Gaseous Electronics Conference, Urbana, IL, 1990 (unpublished), paper NA-5.
[4]J. H. Keller, J. C. Forster, and M. S. Barnes, J. Vac. Sci. Technol. A **11**, 2487 (1993).
[5]M. S. Barnes, J. C. Forster, and J. H. Keller, Appl. Phys. Lett. **62**, 2622 (1993).
[6]J. A. O'Neill, M. S. Barnes, and J. H. Keller, J. Appl. Phys. **73**, 1621 (1993).
[7]R. Patrick, R. Schoenborn, and H. Toda, J. Vac. Sci. Technol. A **11**, 1296 (1993).
[8]J. B. Carter, J. P. Holland, E. Peltzer, B. Richardson, E. Bogle, H. T. Nguyen, Y. Melaku, D. Gates, and M. Ben-Dor, J. Vac. Sci. Technol. B **11**, 1301 (1993).
[9]J. Hopwood, C. R. Guarnieri, S. J. Whitehair, and J. J. Cuomo, J. Vac. Sci. Technol. A **11**, 147 (1993).
[10]J. Hopwood, C. R. Guanieri, S. J. Whitehair, and J. J. Cuomo, J. Vac. Sci. Technol. A **11**, 152 (1993).
[11]J. Hopwood, Appl. Phys. Lett. **62**, 940 (1993).
[12]A. E. Wendt, L. J. Mahoney, and J. L. Shohet, in Proceedings of the 45th Gaseous Electronics Conference, Boston, MA, 1992 (unpublished), paper LB-5.
[13]A. E. Wendt, L. J. Mahoney, and J. L. Shohet, J. Appl. Phys. (to be published).
[14]L. J. Mahoney, A. E. Wendt, E. Barriros, C. J. Richards, and J. L. Shohet, J. Appl. Phys. **76**, 2041 (1994).
[15]J. Stittsworth and A. E. Wendt, *Gaseous Electronics Conference*, Gaithersburg, MD, 1994, paper HA-5 [Bull. Am. Phys. Soc. **39**, 1463 (1994)].
[16]T. Fukasawa, T. Nouda, A. Nakamura, H. Shindo, and Y. Horiike, Jpn. J. Appl. Phys. **32**, 6076 (1993).
[17]T. J. Sommerer and M. J. Kushner, J. Appl. Phys. **71**, 1654 (1992).
[18]P. L. G. Ventzek, R. J. Hoekstra, T. J. Sommerer, and M. J. Kushner, Appl. Phys. Lett. **63**, 605 (1993).
[19]P. L. G. Ventzek, R. J. Hoekstra, and M. J. Kushner, J. Vac. Sci. Technol. B **12**, 461 (1994).
[20]A. Paranjpe, J. Vac. Sci. Technol. A **12**, 1221 (1994).
[21]R. A. Stewart, P. Vitello, and D. B. Graves, J. Vac. Sci. Technol. B **12**, 478 (1994).
[22]R. A. Stewart, P. Vitello, and D. B. Graves, in Proceedings of the 40th American Vacuum Society Symposium, Orlando, FL, November 1993 (unpublished), paper PS-MoA6.
[23]F. Jaeger and L. Berry, Oak Ridge National Laboratory (private communication).
[24]T. Bartel, J. Payne, T. Sterk, R. Wise, D. Lymberopoulos, and D. Economou, in Proceedings of the International Conference on Plasma Science, Sante Fe, NM, June 1994 (unpublished), paper 2C3.
[25]B. W. Yu and S. L. Girschick, J. Appl. Phys. **69**, 656 (1991).
[26]R. Morrow, in *Proceedings of 10th International Conference on Gas Discharges and their Applications* (Swansea, Wales, 1992), p. 900.
[27]P. A. Thompson, *Compressible Fluid Dynamics* (McGraw-Hill, New York, 1972), p. 98 and Appendix E.
[28]T. Bartel, Sandia National Laboratory (private communication).
[29]M. Hayashi, "Recommended Values of Transport Cross Sections for Elastic Collision and Total Collision Cross Section for Electrons in Atomic and Molecular Gases," Nagoya Institute of Technology Report No. IPPJ-AM-19, 1991.
[30]K. Tachibana, Phys. Rev. A **34**, 1007 (1986).
[31]D. Rapp and P. Englander-Golden, J. Chem. Phys. **43**, 1464 (1965).
[32]R. H. McFarland and J. D. Kinney, Phys. Rev. **137**, A1058 (1965).
[33]M. Mitchner and C. Kruger, *Partially Ionized Gases* (Wiley, New York, 1973), Chap. 2.
[34]G. L. Rogoff, J. M. Kramer, and R. B. Piejek, Trans. Plasma Sci. **14**, 103 (1986).
[35]J. B. A. Mitchell, Phys. Rep. **186**, 215 (1990).
[36]D. Economou, private communication of cross sections later reported in Ref. 41, 1993.
[37]L. Vriens, Phys. Lett. **8**, 260 (1964).
[38]S.-B. Zhu, Ph.D. thesis, University of California at San Diego, CA, 1984.
[39]P. K. Leichner and R. J. Ericson, Phys. Rev. A **9**, 251 (1974).
[40]J. Velazco, J. Holts, and D. W. Setzer, J. Chem. Phys. **65**, 3468 (1976).
[41]N. L. Bassett and D. L. Economou, J. Appl. Phys. **75**, 1931 (1994).
[42]D. L. King, L. G. Piper, and D. W. Setzer, Soc. Faraday Trans. **2**, 73, 177 (1976).
[43]D. Smith, N. G. Adams, and E. Alge, J. Phys. B **17**, 461 (1984).
[44]R. E. Olson, J. R. Peterson, and J. Moseley, J. Chem. Phys. **53**, 3391 (1970).
[45]Y. Ikezoe, S. Matsuoka, M. Takebe, and A. Viggiano, *Gas-Phase Ion-Molecule Reaction Rate Constants Through 1986* (Maruzen Company, Tokyo, 1987); analogy to O_2, D_2, H_2.
[46]NIST Chemical Kinetics Database Version 5.0, National Institute of Standards and Technology, Gaithersburg, MD, 1993.
[47]C. Lee, D. Graves, M. Lieberman, and D. Hess, J. Electrochem. Soc. **141**, 1546 (1994).
[48]S. C. Deshmukh and D. J. Economou, J. Appl. Phys. **72**, 4597 (1992).
[49]J. Hirschfelder, C. Curtis, and R. Bird, *Molecular Theory of Gases and Liquids* (Wiley, New York, 1954), Chap. 8.
[50]H. W. Ellis, R. Y. Pai, and E. W. McDaniel, At. Data Nucl. Data Tables **17**, 177 (1976).
[51]K. Greenberg, Sandia National Laboratory (private communication).
[52]P. J. Hargis, K. E. Greenberg, P. A. Miller, J. B. Gerardo, J. R. Torcynski, M. E. Riley, G. A. Hebner, J. R. Roberts, J. K. Olthoff, J. R. Whetstone, R. J. Van Brunt, M. A. Sobolewski, H. M. Anderson, M. Splichal, J. L. Mock, P. Beltzinger, A. Garscadden, R. A. Gottscho, G. Selwyn, M. Dalvie, J. E. Heidenreich, J. W. Butterbaugh, M. L. Brake, M. L. Passow, J. Pender, A. Lujan, M. E. Elta, D. B. Graves, H. H. Sawin, M. J. Kushner, J. T. Verdeyn, R. Horwath, and T. R. Turner, Rev. Sci. Instrum. **65**, 140 (1994).
[53]M. Turner, Phys. Rev. Lett. **71**, 1844 (1993).
[54]M. Barnes, LAM Research Corp. (private communication).
[55]D. K. Coultas and J. H. Keller, European Patent Application No. 0379828, December 1989.
[56]D. Schlosser, LAM Research Corp. (private communication).
[57]Y. Ra and C.-H. Chen, J. Vac. Sci. Technol. A **11**, 2911 (1993).